Journal of Turbulence

ISSN: (Print) (Online) Journal homepage: https://www.tandfonline.com/loi/tjot20

Wall heat flux in supersonic turbulent expansion flow with shock impingement

Fulin Tong, Junyi Duan, Xianxu Yuan & Xinliang Li

To cite this article: Fulin Tong, Junyi Duan, Xianxu Yuan & Xinliang Li (2023) Wall heat flux in supersonic turbulent expansion flow with shock impingement, Journal of Turbulence, 24:9-10, 445-473, DOI: 10.1080/14685248.2023.2260777

To link to this article: https://doi.org/10.1080/14685248.2023.2260777

JOURNAL OF TURBULENCE
2023, VOL. 24, NOS. 9–10, 445–473
https://doi.org/10.1080/14685248.2023.2260777

Wall heat flux in supersonic turbulent expansion flow with shock impingement

Fulin Tong[a], Junyi Duan[b,c], Xianxu Yuan[a] and Xinliang Li[b,c]

[a]State Key Laboratory of Aerodynamics, Mianyang, People's Republic of China; [b]LHD, Institute of Mechanics, Chinese Academy of Sciences, Beijing, People's Republic of China; [c]School of Engineering Science, University of Chinese Academy of Sciences, Beijing, People's Republic of China

ABSTRACT

We perform direct numerical simulations to investigate the characteristics of wall heat flux (WHF) in the interaction of an oblique shock wave at an angle of 33.2° and free-stream Mach number $M_\infty = 2.25$ impinging on supersonic turbulent expansion corners with deflection angles of 0° (flat plate), 6° and 12°. The effect of the expansion on the WHF characteristics is analysed by comparing it to the interaction with the flat plate under the same flow conditions and a fixed shock impingement point. In the post-expansion region, the decreased mean WHF is found to collapse onto the flat plate case when scaled with the mean wall pressure. The statistical properties of the WHF fluctuations, including probability density function, frequency spectra, and space–time correlations, are comparatively analysed. The expansion causes an increase in the occurrence probability of negative extreme events, an enhancement of high-frequency energy, and an inhibition of intermediate-frequency energy. The increased expansion angle also results in a faster recovery of characteristic spanwise length scales and an increase in convection velocity. We use the mean WHF decomposition method in conjunction with bidimensional empirical mode decomposition to quantitatively analyse the impact of expansion on scale contributions. It is demonstrated that the presence of the expansion corner has no significant impact on the decomposed results, but it significantly reduces the contribution associated with outer large-scale structures.

ARTICLE HISTORY
Received 11 June 2023
Accepted 11 September 2023

KEYWORDS
Expansion corner; turbulent boundary layer; shock impingement; wall heat flux

1. Introduction

Due to its practical and theoretical significance, numerous studies have been conducted in the past few decades to explore the interaction between shock waves and turbulent boundary layers (SWTBLI). Dolling [1], Gaitonde [2], Clemens and Narayanaswamy [3] have extensively reviewed the progress made in this field, especially in terms of unsteadiness, heat transfer, skin friction, and turbulence amplification. Despite two commonly studied geometries, a turbulent boundary layer entering a compression corner and a shock wave impinging on a flat-plate turbulent boundary layer, have received much more attention,

CONTACT Xianxu Yuan yuanxianxu@cardc.cn State Key Laboratory of Aerodynamics, 621000, Mianyang, People's Republic of China

the SWTBLI near an expansion corner has been comparatively neglected. This is a crucial building block interaction in inlets at off-design conditions, and its underlying physical mechanisms are yet to be fully understood.

At present, most of the available information on the shock-expansion interaction comes from experimental studies. For example, Chew [4] investigated the interaction near a 6° expansion corner with shock generator angles of 4°, 6°, and 8° at Mach numbers 1.8 and 2.5. He suggested that the reflected shock wave was neutralised by the Prandtl-Meyer expansion when the shock impingement point was located at the corner. Chung and Lu [5] studied the effect of impingement location on mean and fluctuating wall pressure in a Mach 8 turbulent cold flow past a 2.5° or 4.25° expansion corner. They found that the fluctuation peaks were lower and the reduced fluctuation levels were shorter as the shock impingement was moved downstream of the corner. White and Ault [6] analysed the effects of the expansion corner on the separation region in a hypersonic SWTBLI at Mach 11.5. They showed that moving the shock impingement point toward the corner had little effect on the size of the separation region if the downstream edge of the separation region occurred upstream of the corner. More recently, Sathianarayanan and Verna [7] reported surface oil flow visualisation and mean surface pressure measurements for an impinging shock-induced interaction near an expansion corner with side walls at Mach 3.9 to study the effect of variations in geometrical parameters (wedge angle, expansion corner angle, and impingement location). Their experiments showed that increasing the expansion corner angle had a weaker impact on the separation location compared to the wedge angle and impingement location. Experiments have shown that increasing the expansion corner angle cannot completely eliminate separation. Only recently, the present authors used direct numerical simulation (DNS) to investigate the effect of expansion on shock wave and turbulent boundary layer interaction flows. Tong et al. [8] numerically found that increasing the expansion corner angle strongly suppressed low-frequency unsteadiness. Zhang et al. [9] used skin friction decomposition method [10] and bidimensional empirical mode decomposition [11] technique to better understand the expansion effect on mean skin friction generation. They found that the main contribution, turbulence kinetic energy production, was insensitive to the expansion effect, but the negative spatial growth contribution was significantly impacted.

Although the wall heat flux (WHF) in SWTBLI flows has been numerically and experimentally studied for many years and the behaviour of WHF through the interaction region is well documented, most of the studies are focused on compression corner interactions or incident shock interactions. Hayashi et al. [12] measured the fluctuating heat fluxes for both unseparated and separated boundary layer conditions at Mach number of 4. They suggested that the observed intermittency of heat transfer was caused by the separation shock wave oscillation, whereas there was only a sharp peak at the impinging point and no intermittency phenomenon for the unseperated interaction. Schülein [13], who used the quantitative infrared thermography and global interferometry skin-friction techniques to make mean WHF and skin friction measurements in SWTBLI flows at Mach 5.0, noticed that increasing shock strength resulted in a clear difference in the distribution of skin friction and heat transfer and argued the invalidation of the Reynolds analogy. Bernardini et al. [14] did not find any evidence of the influence of the low-frequency shock oscillation on the WHF spectra for their DNS studies of oblique shock-wave/turbulent boundary layer interactions and argued that the turbulence amplification was mainly responsible for the generation of peaking heat. Later, Volpiani et al. [15] investigated effects of a nonadiabtic wall on supersonic shock/boundary-layer interaction and found the strong heat transfer and complex pattern within the interaction region. The DNS performed by Prebie et al. [16] compared the QP85 scaling of Back and Cuffel [17] and the Reynolds analogy for an 8° compression ramp in Mach 7.2 flow and showed that the mean heat transfer scaled better with mean wall pressure, rather than skin friction. Based a scale-based decomposition analysis of the mean WHF, Tong et al. [18] found that the increased WHF downstream of the interaction was mainly associated with the amplified outer large-scale structures. To our knowledge, no DNS studies regarding the mean and fluctuating WHF in the shock-expansion interaction have appeared in the literature so far and our understanding of the expansion effect on the characteristics of WHF in the interaction region is still lack. The purpose of the present work is to fill this gap by performing direct numerical simulations of the interactions with and without an expansion corner, where the expansion effect is isolated.

In this paper, the computational methods and validation of the DNS database are introduced in Section 2. The characteristics of the WHF, including probability density function (PDF), power spectrum, space–time correlations and the mean WHF decomposition, are discussed in Section 3, and conclusions are provided in Section 4.

2. Direct numerical simulations

2.1. Governing equations and numerical methods

The study investigates the supersonic impinging SWTBLI flow near an expansion corner by solving the three-dimensional unsteady compressible conservative Navier-Stokes equations for a perfect gas in curvilinear coordinates. The molecular Prandtl number Pr used is 0.7 and the heat capacity ratio γ is 1.4. The relationship between the viscous stress tensor (σ_{ij}) and the rate-of-strain tensor is defined by the constitutive relations for a Newtonian fluid, while the viscosity coefficient (μ) is calculated using Sutherland's law and the heat flux vector is calculated using Fourier's law. The thermal conductivity coefficient (κ) is computed as $\kappa = \mu C_p/Pr$, where C_p is the heat capacity at constant pressure.

An open-source DNS code (Opencfd-SC) proposed by Li et al. [19] is used to perform the simulations. This code has been successfully validated in previous studies of supersonic and hypersonic flows [20–23]. The governing equations are solved directly using a finite difference method with no modelling enforced. The inviscid flux terms are calculated using a bandwidth-optimized fourth-order weighted essentially non-oscillatory scheme with absolute and relative limiters [24], and the Steger-Warming flux splitting method. The scheme has been examined for its strong robustness and low numerical dissipation in numerous compressible flows with discontinuities. The viscous flux terms are discretized using an eighth-order central difference scheme, and the time integration is done using a third-order explicit Runge–Kutta method [25].

2.2. Flow configuration

The computational domain is illustrated in Figure 1. This does not include the wedge-shaped shock generator. The boundary layer starts as a supersonic laminar flow that is tripped by wall blowing and suction, and eventually develops into a fully developed flat-plate turbulent boundary layer before entering an expansion corner. An oblique shock wave with an angle of 33.2° generated using Rankine-Hugoniot relations at the top boundary of the domain impacts the corner tip (x_s). Throughout the paper, the body intrinsic coordinate system (x, y, z) and the Cartesian coordinate system (X, Y, Z), are used. The origin of the coordinate system (x, y, z) is where the expansion begins, as shown in Figure 1, with the x, y and z axes being coordinates in the streamwise direction along the wall, wall-normal and spanwise directions, respectively. The X, Y and Z axes are the Cartesian axial, normal and spanwise coordinates, having the same origin as x, y and z. Thus, the coordinate system (x, y, z) is the same as (X, Y, Z) in the upstream flat-plate region and the expansion angle (α) is used to perform the coordinate transformation in the downstream expansion region. The flat-plate length is $L_{xu} = 71.1$ mm and the expansion length $L_{xd} = 23.3$ mm. The domain size in the wall-normal direction (y) and spanwise direction (z) is 10 and 4.4 mm, respectively. The origin of the coordinate system (x, y) is set at the tip on the surand the wall blowing and suction region extends from $x_a = -63.5$ mm to $x_b = -50.8$ mm. The free-stream conditions are set based on recent DNS studies of Tong et al. [20,21] and experiments of Dupont et al. [26] These conditions include a Mach number of 2.25, a Reynolds number of 2.5×10^4 per millimetre, and a temperature of 169.44 K. At the reference location $x_{\text{ref}} = -7.6$ mm, the thickness of the upstream turbulent boundary layer is estimated to be $\delta = 1.27$ mm and the corresponding Reynolds number $Re_\delta/\text{mm} = \rho_\infty U_\infty \delta/\mu_\infty = 31750$, where ρ_∞, U_∞ and μ_∞ denote the free-stream density, velocity and viscosity, respectively. In this paper, quantities in the free stream are denoted with the subscript '∞' and quantities at the wall are denoted with the subscript 'w.' The velocity components in the x, y, and z directions are denoted as u, v, and w, respectively. The corresponding velocities in the Cartesian coordinate system are denoted as U, V, and W.

2.3. Simulation setup

This study performs three DNS cases, labelled as FP, EC6 and EC12. Case EC6 involves simulating an oblique shock wave hitting the tip of a 6° expansion corner, and case EC12 corresponds to the simulation of the interaction with a 12° expansion corner, while case FP involves an oblique shock wave interacting with a flat plate (i.e. the deflection angle α is zero). The inflow conditions, domain size, and location of the nominal impingement point are identical for three cases, except the expansion angle. The size of the computational domain and the grid parameters for the three DNS cases are listed in Table 1. The domain is discretized using a grid of $3042 \times 430 \times 340$ points in the x, y, and z directions, respectively. The grid spacing in the z direction is uniform, and the x-y plane grid for case EC12 is shown in Figure 2. The x direction grid points are clustered in the region between −20.3 and 19.6 mm to resolve the shock-expansion interaction. 600 points are progressively refined in the transition zone between −71.1 and −20.3 mm, and 2432 points are evenly spaced in the interaction region. Only 10 points are coarsened in the fringe region at $x > 19.6$ mm. The y direction, grid points are clustered toward the wall and there are approximately 280 points distributed between the wall and boundary layer edge. The present grid resolution in the interaction region is $\Delta x^+ = 8.5$, $\Delta z^+ = 7.15$, $\Delta y^+ = 0.55$ (at the first grid point above the wall), and $\Delta y^+ = 5.5$ (at the boundary layer edge), which is comparable to recent

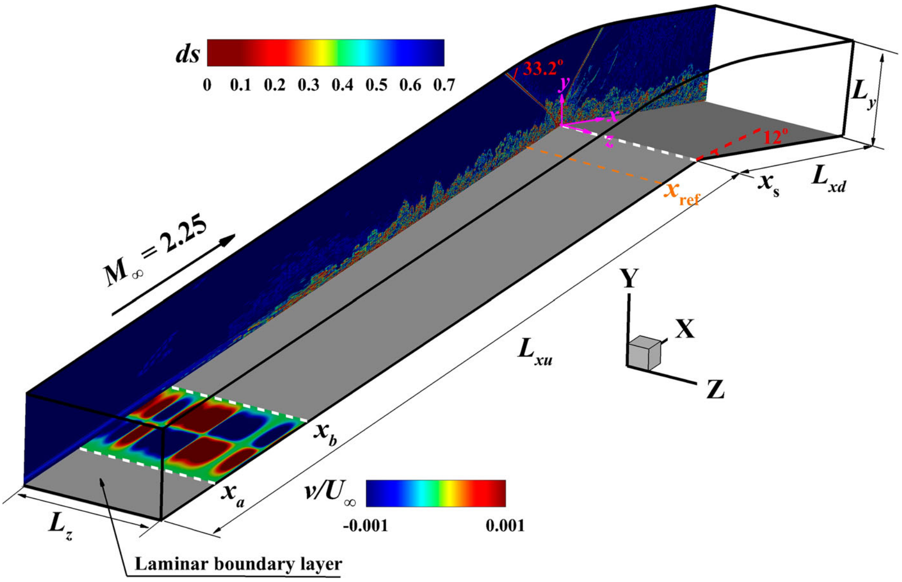

Figure 1. Sketch of the computational domain for the simulation together with contour of the instantaneous density gradient ds in the x–y plane at $z = 0$ and contour of the wall-normal velocity v/U_∞ in the wall blowing and suction region ($x_a < x < x_b$) for EC12.

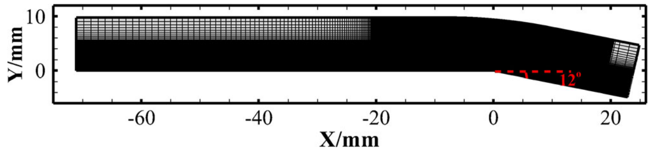

Figure 2. Sketch of the computational grid for EC12. The grid is plotted at intervals of two points in the x direction and five points in the y direction.

Table 1. Numerical parameters for the three DNS cases.

			grid spacing		
Run	Domain size $L_x \times L_y \times L_z$ (mm)	Grid number $N_x \times N_y \times N_z$	Δx^+	Δy^+	Δz^+
FP/EC6/EC12	94.4 × 10 × 4.4	3042 × 430 × 340	8.5	0.55-5.5	7.15

DNS studies of supersonic expansion corner [27] and SWTBLI flows [28]. Unless otherwise stated, the superscript + represents non-dimensionalization by wall units at the reference location x_{ref}.

The computational domain is bounded by a steady laminar boundary layer profile given by Tong et al. [20] at the inlet, supersonic outflow boundary conditions at the outlet, a no-slip isothermal boundary condition at the bottom wall, and a no-reflecting boundary condition at the upper boundary. Further, the two sides are subjected to periodic boundary conditions in the spanwise direction, ensuring spanwise homogeneity of the flow. The wall temperature, $T_{\mathrm{w}} = 254.16$ K, is kept constant, which corresponds to about $0.75T_r$ (with T_r

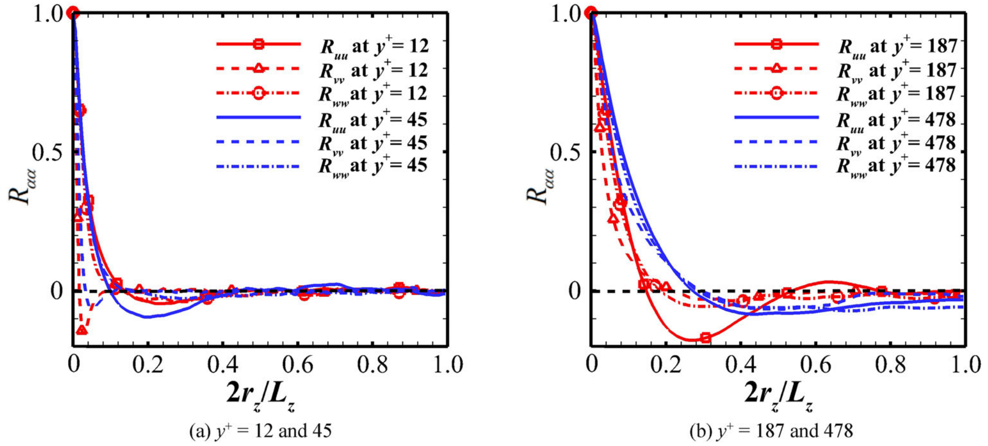

(a) $y^+ = 12$ and 45 (b) $y^+ = 187$ and 478

Figure 3. Two-point correlations of velocity fluctuations as a function of spanwise distance r_z at four wall-normal locations and $(x - x_s)/\delta = 1.5$. (a) $y^+ = 12$ and 45; (b) $y^+ = 187$ and 478

being the recovery temperature). The unsteady wall-normal velocity disturbances added in the wall blowing and suction region ($x_a < x < x_b$) are set in accordance with the DNS studies of Tong et al. [21], where two streamwise modes, 10 spanwise modes, and five temporal modes are introduced in the wall fluctuations, with an amplitude $A = 0.15U_\infty$ and a basic frequency $\varpi = 0.393U_\infty/\delta$.

A total of 600 three-dimensional instantaneous flow fields were sampled at a constant interval as the initial transient flow was washed out after a two-flow-through time period and the statistical steady state was approached. Fully time-resolved wall heat flux signals were collected in the *x*-*z* plane. To accurately estimate the spatial and temporal evolution of the fluctuations, the WHF statistics reported in the following analysis are based on 12,000 flow samples. In the results, the Reynolds average and the Favre (density-weighted) average are denoted by a bar and a tilde, respectively, with the corresponding fluctuations being represented by a prime and a double prime. The mean flow field was obtained using the average in the spanwise direction and over time.

2.4. Validation of DNS data

The present study uses a selected spanwise width of approximately $L_z = 3.2\delta$, which is larger than the typical value of $L_z \approx 2.0\delta$ used in previous numerical studies of SWTBLIs. In Figure 3, we investigate the effect of the selected spanwise width on the DNS results. Following the analysis of Pirozzoli et al. [29], we show the two-point spanwise correlations of velocity fluctuations (R_{uu}, R_{vv}, and R_{ww}) calculated at four wall-normal locations ($y^+ = 12$, 45, 187 and 478) in the shock-expansion region $(x - x_s)/\delta =$ 1.5 as a function of the spanwise width r_z. As expected, increasing r_z leads to a sharp decrease in the correlation coefficient in both the inner and outer layers. The velocity fluctuations are not correlated over a spanwise distance of $L_z/2$, as all the correlation coefficients remain around zero. This confirms that the width used in the current simulation is reasonable and large enough to ensure that turbulence dynamics are not inhibited.

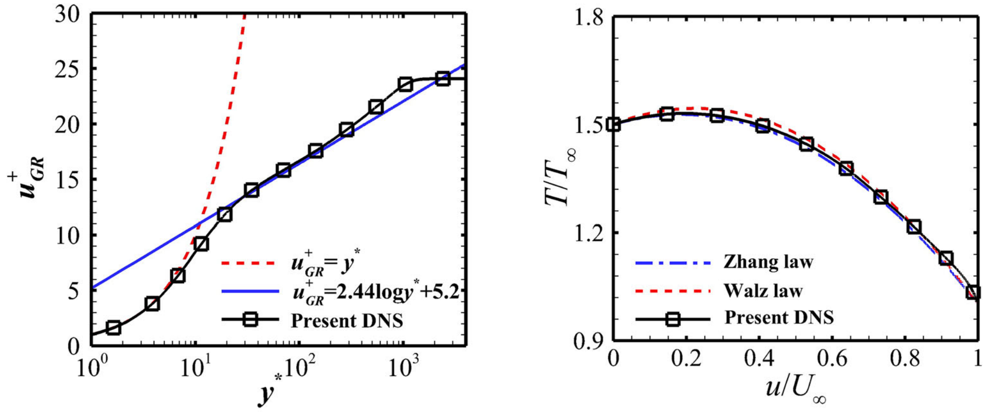

(a) Mean streamwise velocity

(b) Mean temperature

Figure 4. Profiles of mean streamwise velocity $u_{GR}{}^+$ using total-stress-based compressible transformation and mean temperature compared with the laws of Walz [31] and Zhang [32] at x_{ref}. (a) Mean streamwise velocity; (b) Mean temperature

To validate the inflow turbulence generated by the laminar-to-turbulent transition, Figure 4(a-b) shows the mean streamwise velocity profile and the mean temperature-velocity relation at the reference location x_{ref}, respectively. In Figure 4(a), the total-stress-based transformation, proposed by Griffin et al. [30], is applied, where the transformed velocity $u_{GR}{}^+ = \int S_t{}^+ dy*$ is plotted against the semilocal wall-normal coordinate $y^* = y/\ell_{sl}$, with $S_t{}^+$ and ℓ_{sl} denoting the generalised nondimensional mean shear and the semilocal length scale, respectively. Clearly, the computed mean streamwise velocity, $u_{GR}{}^+$, agrees well with theoretical predictions in the viscous layer for $y* < 6$ and in the log-law region for $30 < y^* < 100$, demonstrating high resolution in the current simulation. In Figure 4(b), reasonable agreement with the classic Walz solution [31] and the generalised Reynolds analogy proposed by Zhang et al. [32] is obtained, suggesting that the computed mean temperature profile at x_{ref} is in an equilibrium state. On the other hand, the wall-normal profiles of the density-scaled root-mean-square velocity fluctuations (RMS$^+$) at the reference location x_{ref} reported in Figure 5(a-b) are plotted in inner and outer coordinates, respectively, where the compressible DNS results of Pirozzoli et al. [33] and Sandloo et al. [34] and the experimental data of Humble et al. [35] and Piponniau et al. [36] at comparable Reynolds numbers are also included. It is apparent that that the computed profiles compare reasonably with previous data and the streamwise component reaches its maximum value around 2.9 at $y/\delta \approx 0.018$ (or $y^+ \approx 14$). It is confirmed that the turbulent fluctuations inside the entire boundary layer are well resolved.

Moreover, the chosen grid resolution has been assessed by conducting a grid-sensitivity study and examining the mean wall properties across the shock-expansion interaction. The refined grid used in the simulation has 50% more nodes in both the x and z directions compared to the baseline grid. Figure 6(a–c) compares the mean wall pressure P_w, wall skin friction coefficient $C_f = \mu \partial u/\partial y|_w$, and Stanton number $St = \kappa \partial T/\partial y|_w/\rho_\infty U_\infty C_p(T_w\text{-}T_r)$ for the two grids and shows that they are insensitive to the refinement. It is seen that the overall wall pressure evolution in the interaction region is slightly changed and the streamwise locations of the mean separation and reattachment points ($C_f = 0$) for the two

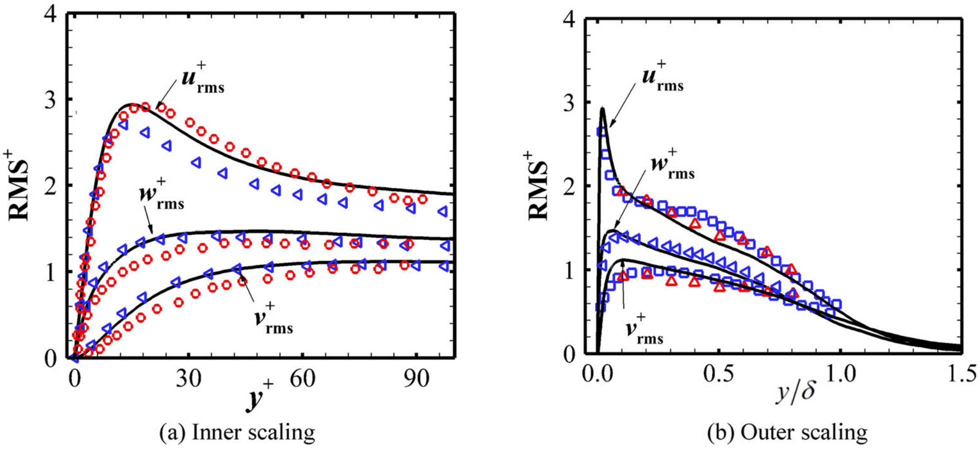

Figure 5. Distributions of density-scale turbulence intensities RMS$^+$ at x_{ref}. Lines: present DNS; left triangles: Pirozzoli et al. [33]; circles: Shadloo et al. [34]; triangles: Humble et al. [35]; squares: Piponniau et al. [36]. (a) Inner scaling; (b) Outer scaling

grids are nearly undistinguishable, where relatively larger deviations (less than 9%) are only observed at $-1 < (x - x_s)/\delta < 0$ for the mean Stanton number, supporting that the present grid resolution is sufficient to provide grid-converged results. For other cases, similar grid convergence has been checked but not reported here for simplicity.

Overall, the above domain- and grid-sensitivity analyses have shown that the interaction near an expansion corner is accurately resolved by the present grid resolution with a domain width of about $L_z = 3.2\delta$. The good agreement with the well-accepted numerical and experimental data is obtained for the mean flow and fluctuation statistics and it can be said that the present laminar-to-turbulent transition method is of high reliability and a fully developed equilibrium turbulence state upstream of the shock-expansion interaction region is generated as desired.

3. Results and discussion

3.1. Instantaneous and mean flow fields

In Figure 7, the expansion effect on the flow pattern in the interaction region is compared qualitatively using contour plots of the instantaneous temperature field T/T_∞ in the x-y mid-plane. As previously seen in DNS studies by Pirozzoli et al. [37] and Priebe et al. [38], the visualisation for FP shows a complex shock wave system related to the impinging shock and an amplification of turbulence fluctuations downstream of the interaction. The visualisations for EC6 and EC12 illustrate that the impinging shock still interacts with the reflected shock, indicating that the presence of the expansion corner does not alter the typical topology of SWTBLI flows. However, the reflected shock originating from the interaction becomes weaker, and the temperature at $(x - x_s)/\delta > 0$ decreases dramatically in both the main stream and the reattached boundary layer. This suggests that significantly reduced turbulence intensities are mostly dominant in the shock-expansion region, largely due to the strong favourable pressure gradient induced by the expansion.

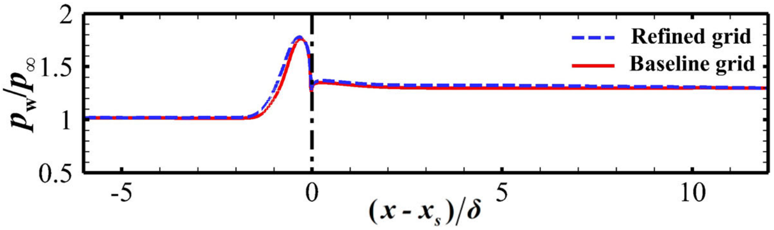

(a) Wall pressure

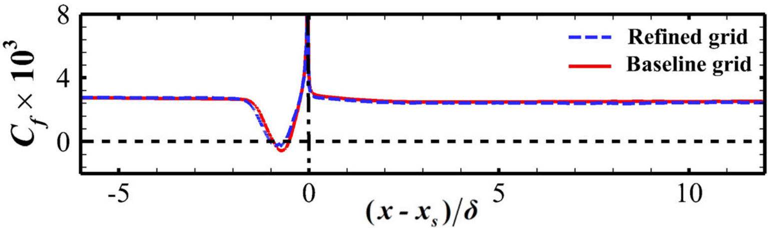

(b) Skin friction coefficient

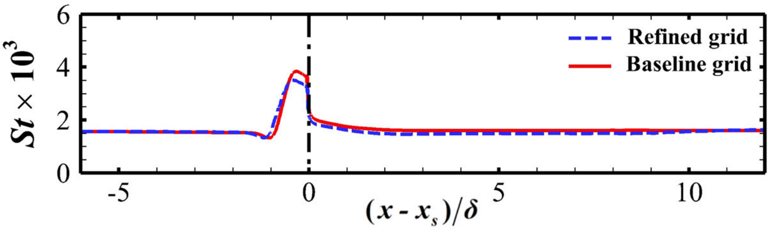

(c) Stanton number

Figure 6. Grid-sensitivity study with respective to mean wall quantities for EC12. (a) Wall pressure; (b) Skin friction coefficient; (c) Stanton number.

Figure 8 shows a qualitative view of the impact of expansion on the instantaneous WHF field from a top perspective. In the results that follow, the wall heat flux C_h is calculated as $C_h = \kappa \partial T/\partial y|_{\mathrm{w}}$. It is evident that the upstream streaky pattern is mostly preserved downstream of the interaction region for all cases. However, the most notable difference between the three DNS cases is a significant decrease in the magnitude of the WHF. As we can see, the WHF for FP is mainly dominated by flow patches with high positive C_h, which are frequently observed upstream and downstream of the impingement point x_{s}. In the other two cases, it is clear that the large positive C_h is not present at $(x - x_{\mathrm{s}})/\delta > 0$ as the expansion angle is increased, and only a small region of high positive value is observed at $-1 < (x - x_{\mathrm{s}})/\delta < 0$, suggesting an essential decrease in the WHF field due to the imposed expansion effect.

Figure 9(a) quantitatively compares the mean WHF throughout the interaction for all the cases. As seen, the mean C_h for FP experiences a slight decrease after entering the interaction zone, followed by a sharp increase close to the impingement point x_{s}. In the downstream relaxation region, it exhibits a slow decrease and reaches a nearly constant level at $(x - x_{\mathrm{s}})/\delta > 5$, which is about 1.8 times larger than the upstream equilibrium value. These trends are similar to previous findings by Volpiani et al. [15] and Hayashi

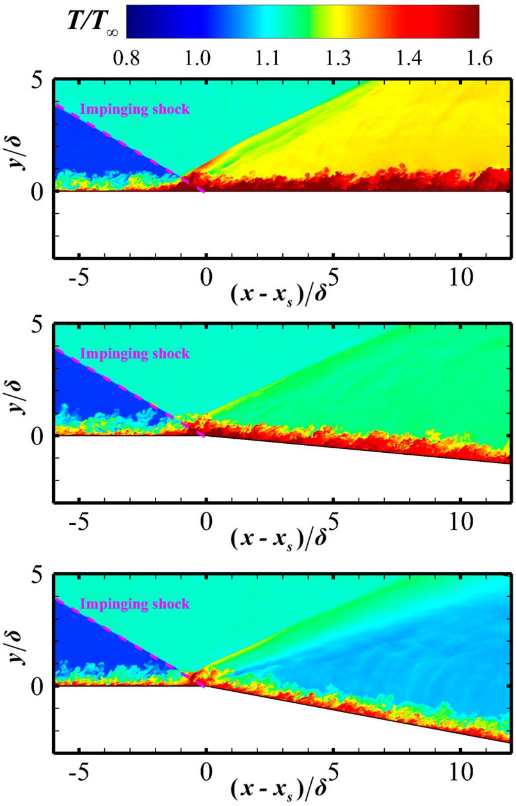

Figure 7. Contours of instantaneous temperature field T/T_∞ in the x-y mid-plane: cases FP, EC6, and EC12 from top to bottom.

et al. [12] in the case of impinging SWTBLIs. The main influence of expansion on the mean C_h distribution is mostly reflected by a downstream shift of the sharp increase in the streamwise location, associated with a reduction in the separation bubble size, and a sudden drop immediately in post-expansion region, related to the significantly weakened large-scale structures in the expansion process. It is important to emphasise that despite the decreased mean C_h for EC12 collapsing onto the upstream value at $(x - x_s)/\delta > 2$, the contributions of turbulent coherent structures with different length scales to the mean C_h generation are not the same as the values in the upstream turbulent boundary layer. This point will be discussed further in the next scale decomposition of the mean WHF. Moreover, the impact of expansion on turbulence downstream of the interaction can be further understood from Figure 9(b), where the wall-normal profiles of the mean turbulent kinetic energy at three streamwise locations s_1-s_3 (see Figure 8) are reported. Compared to FP, the inner peak at $y/\delta < 0.01$ is relatively unchanged, whereas the amplified peak value in the outer region is significantly decreased at $y/\delta > 0.1$. Clearly, increasing the expansion angle induces a consistent reduction in the magnitude of the outer peak, whereby the inner peaks become dominant at locations s_1-s_3 for EC12, being more similar to that of the upstream boundary layer, and the differences between the three profiles are negligible, implying a faster recovery of turbulence in the downstream region.

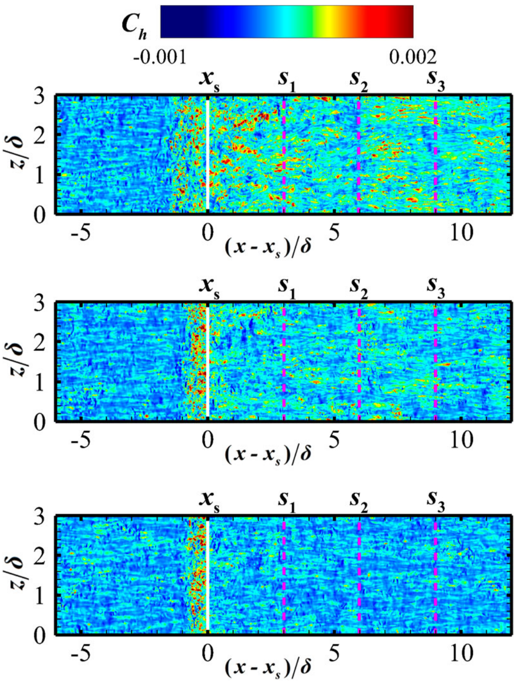

Figure 8. Contours of instantaneous WHF C_h in the wall plane: cases FP, EC6, and EC12 from top to bottom. Locations s_1–s_3: $(x - x_s)/\delta = 3, 6$, and 9.

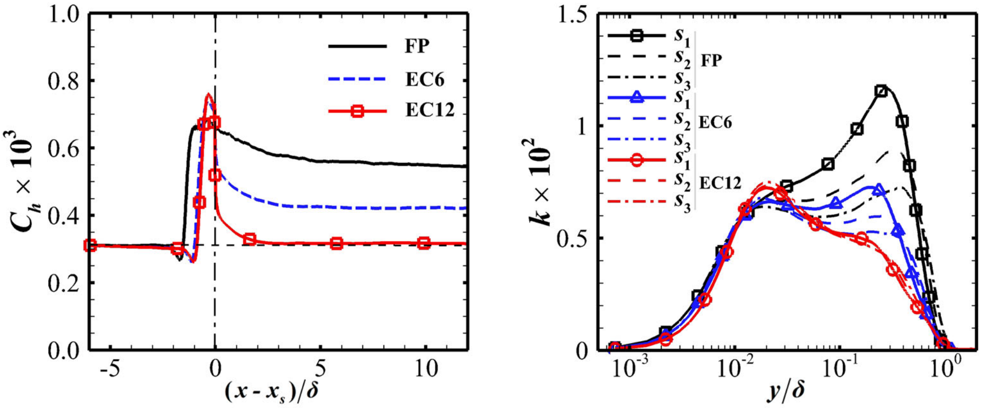

(a) Mean WHF

(b) Mean turbulent kinetic energy

Figure 9. (a) Streamwise distributions of mean WHF C_h and (b) wall-normal distributions of mean turbulent kinetic energy $k = \widetilde{u''_i u''_i}/2$ at various selected locations.

To better verify the link between the mean Stanton number St and the mean wall skin friction coefficient C_f, we have analysed the distribution of the Reynolds analogy factor (RAF $= 2St/C_f$), reported in Figure 10(a). In the upstream of the interaction, the value of RAF is approximately 1.14, whereas RAF deviates significantly from its upstream value for

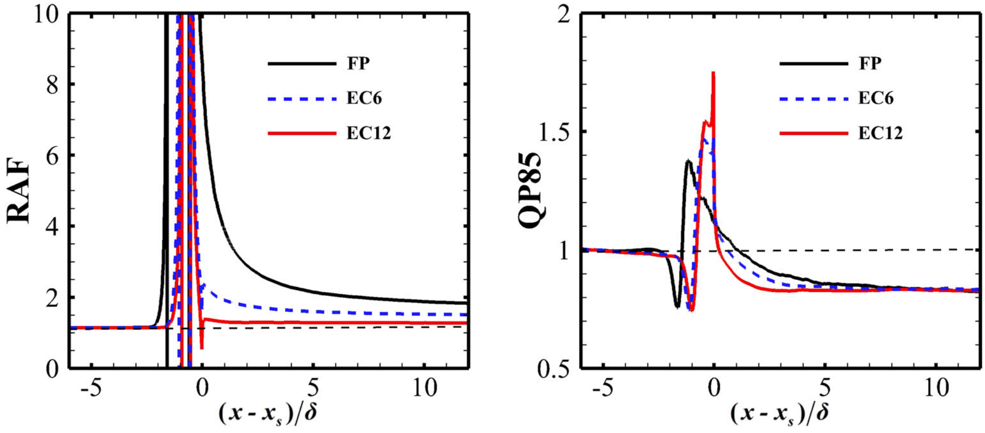

(a) Reynolds analogy factor (RAF)

(b) QP85 scaling

Figure 10. Streamwise distributions of (a) Reynolds analogy factor (RAF) and (b) QP85 scaling.

all cases due to negative C_f in the separation region $-2 < (x - x_s)/\delta < 0$. In the downstream region, the Reynolds analogy factor experiences a slow decay, approaching RAF $\approx$ 1.84 at $(x - x_s)/\delta = 12$ for FP, while it remains constant at RAF $\approx$ 1.52 for EC6 and at RAF $\approx$ 1.27 for EC12. In Figure 10(b), the distribution of the QP85 scaling, which links the mean wall heat flux C_h to the mean wall pressure P_w, is reported. According to the analysis of Back and Cuffel [39] in hypersonic SWTBLI flows, the QP85 scaling is defined as $\text{QP85} = (C_h/C_u)(P_u/P_w)^{0.85} \approx \text{const} \approx 1$, where C_u and P_u denote the upstream mean WHF and wall pressure, respectively. As we can see, the value of QP85 in the upstream boundary layer is approximately 1.0, which is consistent with previous findings reported by Roy and Blottner [40] and Priebe et al. [16] for compressible zero pressure gradient turbulent boundary layers. It is clear that the QP85 scaling varies between 0.76 and 1.37 throughout the interaction region for FP, which is between 0.74 and 1.76 for EC6 and EC12. Another important observations are the excellent collapse of the three QP85 curves and a nearly constant value $\text{QP85} = 0.83$ observed at $(x - x_s)/\delta > 8$, further supporting that the mean C_h is better scaled with the mean wall pressure P_w.

3.2. Probability density function

The PDFs of WHF at various streamwise locations, normalised by the local mean value $C_{h,\text{av}}$, are shown in Figure 11 on a logarithmic scale for both cases. Similar to the wall shear stress PDF analysis performed by Daniel et al. [41] for zero pressure gradient boundary layers, this normalisation leads to a better collapse of the positively skewed PDFs at the three locations. The differences in the positive tails of the three PDFs for the three DNS cases are negligible, whereas the negative tails of the EC12 simulation become much wider compared to those of the EC6 simulation, which are much closer to the upstream negative tail at x_{ref}. This suggests that the occurrence probability of extreme negative events of C_h in the downstream region is significantly increased by the expansion process, resulting in a faster recovery of negative WHF for EC12.

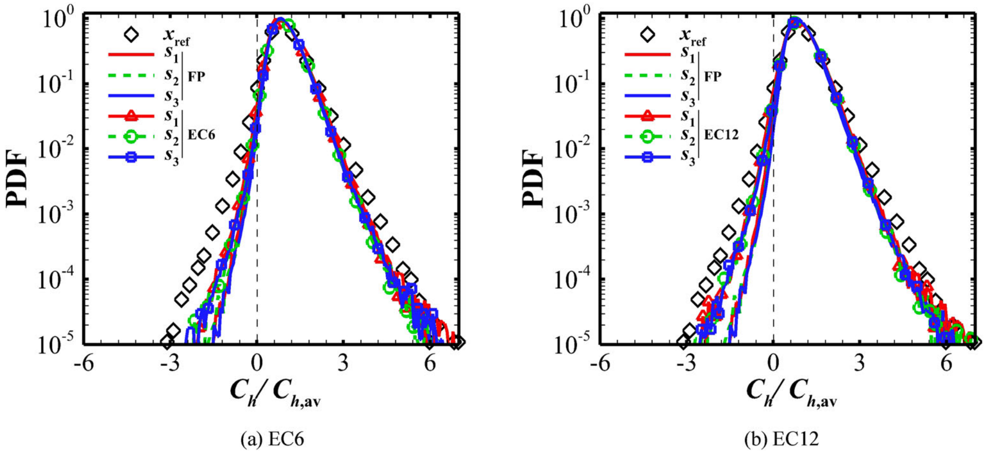

(a) EC6

(b) EC12

Figure 11. PDFs of the WHF C_h normalised by the local mean value $C_{h,\mathrm{av}}$ at various streamwise locations.

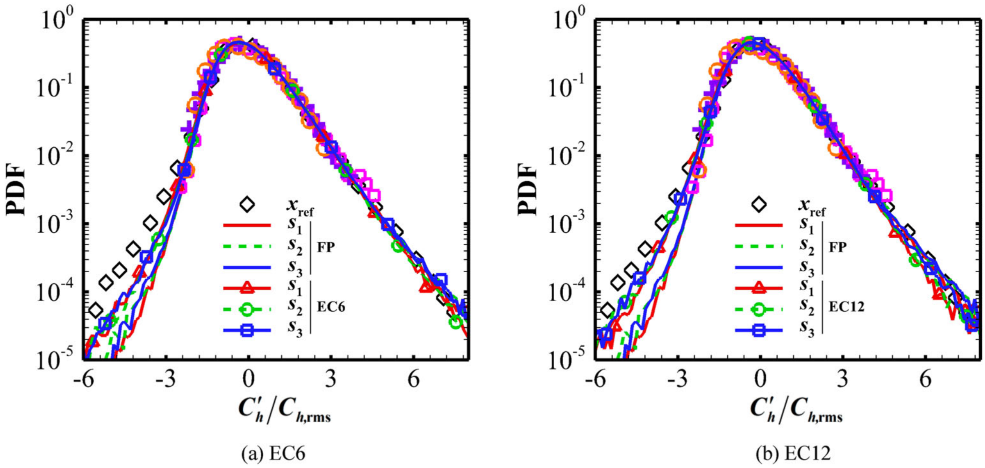

(a) EC6

(b) EC12

Figure 12. PDFs of the WHF fluctuations ($C_h{}'$) normalised by the local RMS value $C_{h,\mathrm{rms}}$ at various streamwise locations. Squares: Grosse and Schröder [42]; crosses: Nottebrock et al. [43]; circles: Sreenivasan and Antonia [44].

Figure 12 compares the probability density functions of the fluctuating WHF (C'_h) normalised by the local RMS value ($C_{h,\mathrm{rms}}$), at different streamwise locations for all cases. The measurements of the fluctuating wall shear stress in wall bounded flows, reported by Grosse and Schröder [42], Nottebrock et al. [43] and Sreenivasan and Antonia [44], are also included for comparison. Clearly, the similarities between the normalised PDFs of C'_h at locations s_1-s_3 are evident. The positive tails of the negatively skewed PDFs collapse well, while the negative tails are affected by the change in the corner angle and become wider than those for FP, gradually approaching to the upstream value at x_{ref}. It is important to note that, under this normalisation, all the PDFs of the WHF fluctuations between $C'_h/C_{h,\mathrm{rms}} = -2$ and 4 agree well with previous PDFs of the wall shear stress fluctuations.

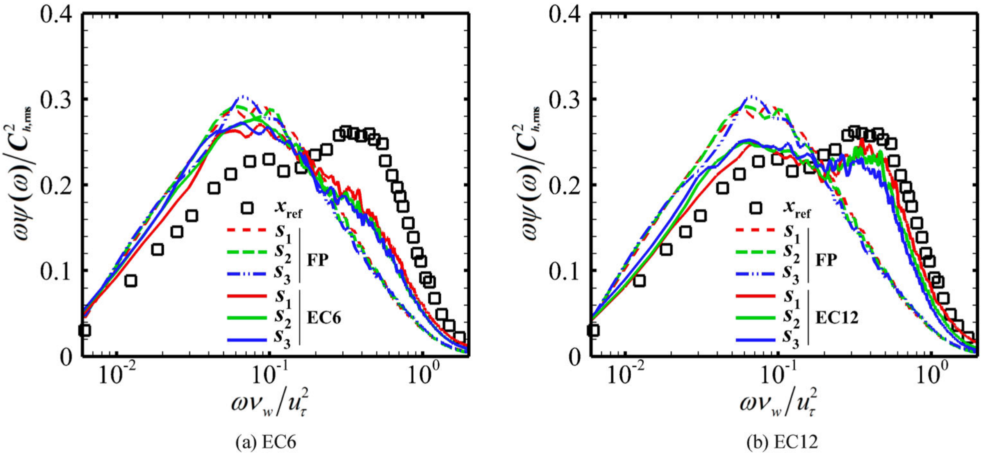

Figure 13. Pre-multiplied spectra of the WHF fluctuations at various streamwise locations for (a) EC6 and (b) EC12.

3.3. Spectral analysis

To further understand the impact of expansion on the frequency distribution of the fluctuating WHF, the pre-multiplied spectra $\omega\Psi(\omega)$ at locations s_1-s_3 are shown in Figure 13(a) and 13(b) for EC6 and EC12, respectively, where the results from the FP case are also included. The spectra are plotted as a function of the normalised angular frequency $\omega\upsilon_w/u_\tau{}^2$, with normalisation based on the square of the local root mean square (RMS) value $C_{h,\mathrm{rms}}$. For better comparison, both the kinematic viscosity at the wall υ_w and the friction velocity u_τ are taken at x_{ref}. To estimate the power spectral density $\Psi(\omega)$ of WHF fluctuations, the WHF signal is analysed using Welch's algorithm with a hamming window. The signal is divided into nineteen segments with a 50% overlap and the spectra are then averaged in the spanwise direction.

The obtained WHF spectra upstream of the interaction are primarily dominated by a peak frequency centred at $\omega\upsilon_w/u_\tau{}^2 \approx 0.5$ and have considerable energy at lower frequencies $\omega\upsilon_w/u_\tau{}^2 < 0.1$. For FP, it is seen that the spectra at locations s_1-s_3 have a different shape compared to the results at x_{ref}. The intermediate-frequency components of the spectra become stronger at $\omega\upsilon_w/u_\tau{}^2 < 0.2$, whereas the high-frequency energy levels are relatively weakened, which results in a shift of the peak frequency to lower values of $0.04 < \omega\upsilon_w/u_\tau{}^2 < 0.08$ in the downstream relaxation region. Bernardini et al. [14] previously found a similar behaviour for supersonic SWTBLI flows and suggested that the shift toward intermediate frequencies may be associated with the shedding of vertical structure in the separated shear layer. As shown in Figure 13(a), the spectra for EC6 exhibit a similar behaviour, whereas the expansion effect is mainly reflected by the attenuation of the intermediate-frequency components and the enhancement of the high-frequency components, suggesting a slow recovery of the WHF spectra downstream of the expansion. It can be seen from Figure 13(b) that the increased expansion effect causes a large decrease in intermediate energy and a remarkable increase in high-frequency energy, leading to the spectra in the post-expansion region similar to that at x_{ref}, except for two comparable spectral bumps in the spectra. The reason for this trend is not clear, but it may be linked to the

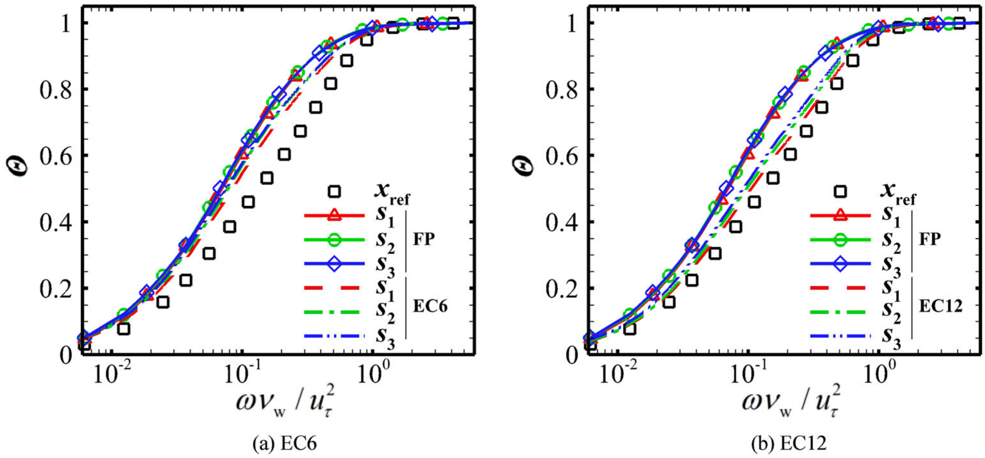

(a) EC6 (b) EC12

Figure 14. Integration of the WHF spectra for (a) EC6 and (b) EC12.

mixing-layer induced vortical structures [14,45–47], that convect downstream and have not fully recovered in the post-expansion region, which are responsible for most of the WHF fluctuations and still have larger scales than those in the upstream turbulent boundary layer. It is suggested that the recovery of the WHF spectra is greatly accelerated as the deflection angle is increased.

In Figure 14, the variation of the frequency distribution induced by the expansion effect is further quantified by integrating the power spectral density below a specific frequency, which is defined as.

$$\Theta = \int_0^{\omega} \Psi(\zeta) d\zeta. \tag{1}$$

It is evident in Figure 14(a) that all the three curves for EC6 are shifted to the left side of the figure in comparison to the x_{ref} curve, very close to curves for FP, confirming the predominance of the intermediate-frequency components for FP and EC6. However, the trend reported in Figure 14(b) is different, where the three curves for EC12 are clearly shifted to the right side of the figure, indicating that an increase in the importance of high-frequency components downstream of the expansion. According to the above analysis in Figure 13, the range of $\omega \upsilon_{\text{w}}/u_\tau{}^2 > 0.2$ is reasonably classified as the high-frequency component. It can be seen that nearly 40% of the spectral energy is stored at x_{ref}, and the corresponding values at location s_3 are about 20% and 26% for FP and EC6, respectively, whereas it is increased to be about 33% for EC12.

3.4. Space–time correlations

To examine the impact of expansion on the spatial and temporal evolutions of the fluctuating WHF, we analyse the two-point space–time correlation coefficient R_{cc}. This is defined as.

$$R_{cc}(\Delta x, \Delta z, \Delta t) = \frac{\overline{C'_h(x, z, t) C'_h(x + \Delta x, z + \Delta z, t + \Delta t)}}{C_{h,\text{rms}}(x) C_{h,\text{rms}}(x + \Delta x)}, \tag{2}$$

where Δt, Δx and Δz represent the time delay, streamwise, and spanwise spatial separations, respectively.

Figure 15 displays the iso-lines of the two-point correlation coefficient R_{cc} (Δx^+, Δz^+, 0) for the three DNS cases at locations s_1-s_3. The results taken at x_{ref} are included for direct comparison. All the contour maps exhibit a streamwise elongated distribution, which supports the qualitative observations in Figure 8 that the streaky structures are essentially unaffected by expansion. However, differences between the three cases are evident. For FP, it is seen that as the probe moves downstream, the streamwise spatial coherence of the WHF field increases consistently, whereas the spanwise coherence slightly decreases. For example, at location s_1, the spatial extents based on a correlation level of 0.3 are $\Delta x^+ = 232$ and $\Delta z^+ = 70$ in the x and z directions, respectively. At location s_3, the values are $\Delta x^+ = 292$ and $\Delta z^+ = 54$, respectively. For EC6 and EC12, a different behaviour is observed, where the correlation maps at locations s_1-s_3 are nearly indistinguishable and the differences at larger streamwise separations become negligible as the expansion angle increases. In particular, good collapse onto the reference contour map taken at x_{ref} is achieved in the spanwise direction, while the streamwise extent of the WHF field in the expansion region for EC12 is still larger than that at x_{ref}, indicating that the recovery of the characteristic spanwise length scales in the post-expansion region is very faster than that of the streamwise length scales.

The iso-lines of the space–time correlation coefficient $R_{cc}(\Delta x^+, 0, \Delta t^+)$ at locations s_1-s_3 for the three DNS cases are shown in Figure 16, respectively, and compared to the contour map at x_{ref}. The incoming turbulent boundary layer features a highly narrowed elliptical distribution, with forward-leaning major axes in the first and third quadrants of the Δt^+-Δz^+ plane, typical of the downstream propagation of the fluctuating WHF. This convective nature is similar to previous numerical findings in wall pressure and wall shear stress fluctuations reported by Bernaridini et al. [48] and Daniel et al. [41] for wall-bounded flows. As we can see, the spatial and temporal extents of the correlation contours are relatively insensitive to the imposed expansion effect, but the overall inclination of the maps varies significantly, showing that the convection velocity of WHF fluctuations downstream of the interaction is strongly affected by the increased expansion. For FP, the figure shows a decrease in inclination angle of the major axes from the axis of delay time, whereas the results of EC6 and EC12 show a considerable increase, hinting at a systematic recovery of convection velocity in the downstream region.

Regarding the increased expansion effect on the convection velocity of the WHF fluctuations, further evidence is presented in Figure 17. The figure shows the calculated local convection velocity, u_c/U_∞, as a function of the time delay Δt^+. As suggested by Duan et al. [49], the convection velocity, defined as the ratio $\Delta x^+/\Delta t^+$, is computed at a given time delay Δt^+, and at the value of Δx^+ where $R_{cc}(\Delta x^+, 0, \Delta t^+)$ attains its local maximum value. The figure suggests that the WHF fluctuations at x_{ref} propagate at a speed in the range of $0.55-0.62U_\infty$. However, a significant decrease is clearly found for FP, with the convection velocities at locations s_1-s_3 varying between $0.2U_\infty$ and $0.4U_\infty$. More importantly, near collapse of the u_c distributions is both observed for EC6 and EC12, where the fluctuations propagate at a larger speed in the ranges of 0.3-$0.45U_\infty$ for EC6 and 0.45-$0.52U_\infty$ for EC12, confirming that the increased expansion effect significantly increases the convection velocity downstream of the interaction. This trend is very similar to the DNS studies of the WHF fluctuations in a supersonic turbulent expansion corner without an impinging

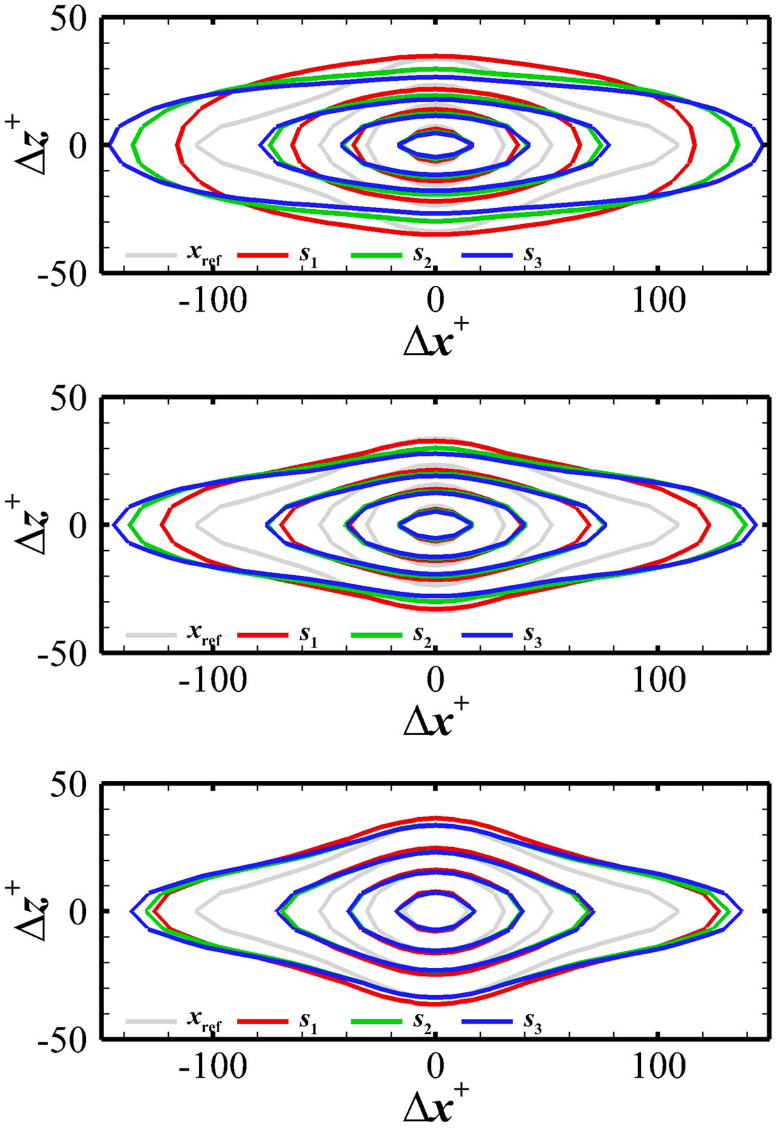

Figure 15. Contour lines of the two-point WHF correlation coefficient $R_{cc}(\Delta x^+, \Delta z^+, 0)$ with four contour levels ($R_{cc} = 0.3; 0.5; 0.7; 0.9$) at various streamwise locations: cases FP, EC6, and EC12 from top to bottom.

shock interaction, as reported by Tong et al. [21], who found that the increased convection velocities in the expansion region are much larger than those at the upstream zero pressure gradient turbulent boundary layer.

3.5. Decomposition of mean WHF

To comprehend the physical process associated with the observed reduction of the mean WHF in the downstream expansion region, a scale-based decomposition analysis was

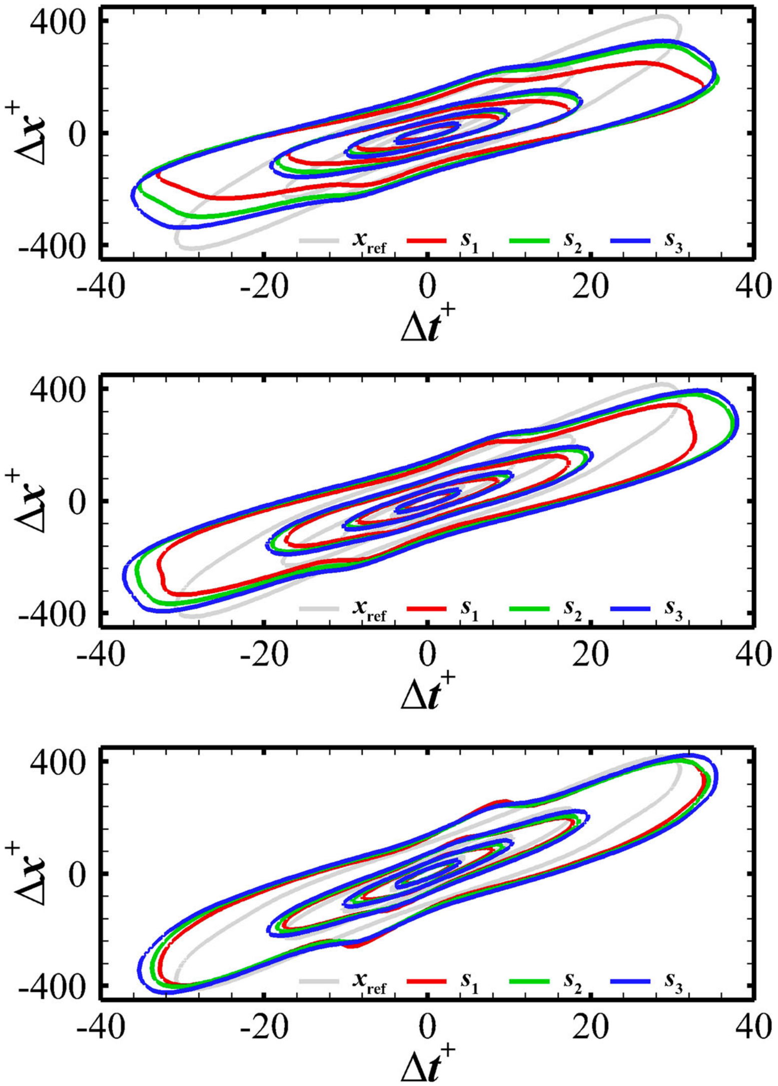

Figure 16. Contour lines of the space-time WHF correlation coefficient $R_{cc}(\Delta x^+, 0, \Delta t^+)$ with four contour levels ($R_{\rm cc} = 0.3; 0.5; 0.7; 0.9$) at various streamwise locations: cases FP, EC6, and EC12 from top to bottom.

conducted to identify the turbulent structures responsible for generating the mean WHF. Only decompositions from FP and EC12 are presented hereafter. Under the assumption of spanwise homogeneity, the decomposition formula for the mean WHF C_h was derived from the integration of the compressible total energy equation. This formula was first developed by Sun et al. [50] and is expressed as follows:

$$C_h = C_{h,C} + C_{h,TH} + C_{h,MD} + C_{h,TKE} + C_{h,MS} + C_{h,RS} + C_{h,G}, \tag{3}$$

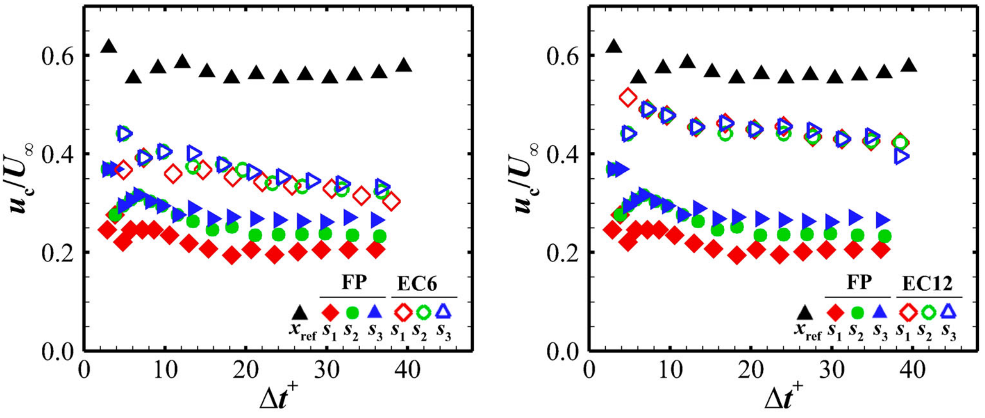

(a) EC6

(b) EC12

Figure 17. Local convection velocity u_c/U_∞ as a function of time delay Δt^+ for (a) EC6 and (b) EC12.

where

$$C_{h,\mathrm{C}} = \frac{1}{\rho_\infty u_\infty^4}\int_0^\infty k\frac{\partial\bar{T}}{\partial y}\frac{\partial\tilde{u}}{\partial y}\mathrm{d}y, \tag{4}$$

$$C_{h,TH} = \frac{1}{\rho_\infty u_\infty^4}\int_0^\infty -c_p\bar{\rho}\widetilde{v''T''}\frac{\partial\tilde{u}}{\partial y}\mathrm{d}y, \tag{5}$$

$$C_{h,\mathrm{MD}} = \frac{1}{\rho_\infty u_\infty^4}\int_0^\infty (\overline{u''\sigma_{xy}} + \overline{v''\sigma_{yy}})\frac{\partial\tilde{u}}{\partial y}\mathrm{d}y, \tag{6}$$

$$C_{h,\mathrm{TKE}} = \frac{1}{\rho_\infty u_\infty^4}\int_0^\infty -\frac{1}{2}(\overline{\rho u''u''v''} + \overline{\rho v''v''v''})\frac{\partial\tilde{u}}{\partial y}\mathrm{d}y, \tag{7}$$

$$C_{h,\mathrm{MS}} = \frac{1}{\rho_\infty u_\infty^4}\int_0^\infty (\tilde{u}\bar{\sigma}_{xy} + \tilde{v}\bar{\sigma}_{yy})\frac{\partial\tilde{u}}{\partial y}\mathrm{d}y, \tag{8}$$

$$C_{h,\mathrm{RS}} = \frac{1}{\rho_\infty u_\infty^4}\int_0^\infty -\bar{\rho}(\tilde{u}\widetilde{u''v''} + \tilde{v}\widetilde{v''v''})\frac{\partial\tilde{u}}{\partial y}\mathrm{d}y, \tag{9}$$

$$\begin{aligned} C_{h,\mathrm{G}} = {} & \frac{1}{\rho_\infty u_\infty^4}\int_0^\infty (\tilde{u} - u_\infty)\rho\frac{D\tilde{E}}{Dt}\mathrm{d}y + \frac{1}{\rho_\infty u_\infty^4}\int_0^\infty (\tilde{u} - u_\infty)[\frac{\partial(\tilde{u}\bar{p})}{\partial x} + \frac{\partial(\tilde{v}\bar{p})}{\partial y}]\mathrm{d}y \\ & - \frac{1}{\rho_\infty u_\infty^4}\int_0^\infty (\tilde{u} - u_\infty)(k\frac{\partial\bar{T}}{\partial x} - c_p\bar{\rho}\widetilde{u''T''} + \overline{u''\sigma_{xx}} + \overline{v''\sigma_{yx}} \\ & - \frac{1}{2}\overline{\rho u''u''u''} - \frac{1}{2}\overline{\rho v''v''u''} \\ & + \tilde{u}\bar{\sigma}_{xy} + \tilde{v}\bar{\sigma}_{yy} - \tilde{u}\overline{\rho u''u''} - \tilde{v}\overline{\rho v''u''})\mathrm{d}y. \end{aligned} \tag{10}$$

Here, the terms $C_{h,\mathrm{C}}$, $C_{h,\mathrm{TH}}$, $C_{h,\mathrm{MD}}$, $C_{h,\mathrm{TKE}}$, $C_{h,\mathrm{MS}}$, and $C_{h,\mathrm{RS}}$ respectively account for contributions associated with heat conduction, turbulent transport of heat, molecular diffusion, turbulent transport of turbulent kinetic energy, the work of molecular stresses, and the work of Reynolds stresses. The term $C_{h,\mathrm{G}}$ represents a combined effect of the variation of specific total energy $\tilde{E}$ with time, the work of pressure, and streamwise heterogeneity.

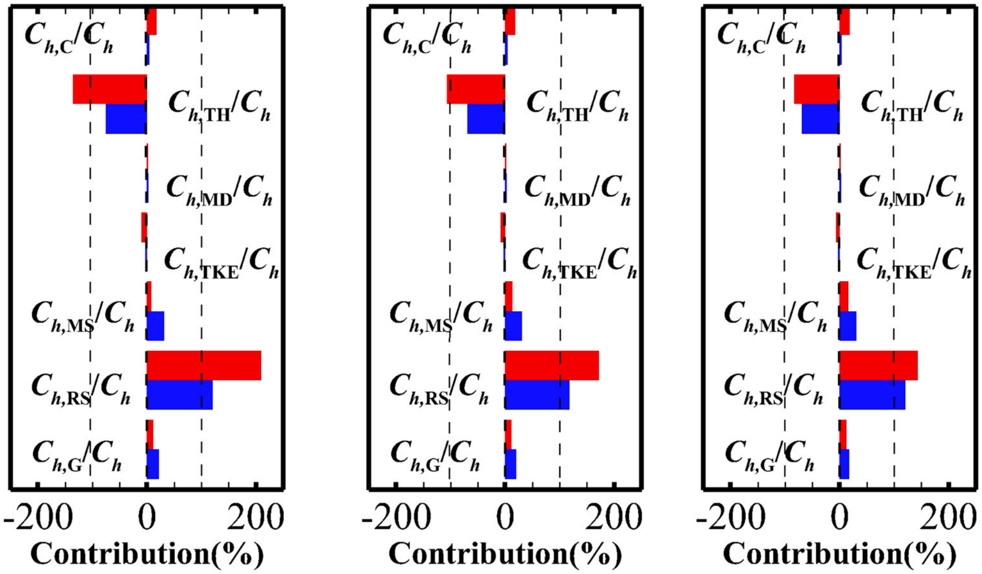

(a) s_1 (b) s_2 (c) s_3

Figure 18. Contributions to mean WHF C_h at locations s_1-s_3 for FP (red) and EC12 (blue). (a) s_1; (b) s_2; (c) s_3

Figure 18 displays the seven decomposed contributions at locations s_1-s_3. It is noteworthy that the total of the seven contributions at all locations deviates approximately 1% from the mean WHF C_h, calculated using the temperature gradient, demonstrating the high reliability of the current decomposition. As shown, the balance between a substantial positive $C_{h,\mathrm{RS}}$ and a substantial negative $C_{h,\mathrm{TH}}$ dominates in both cases, while the remaining five contributions are insignificant due to their small magnitudes. This suggests that C_h generation is mainly driven by the Reynolds stresses work and the turbulent transport of heat, which is insensitive to the expansion effect. Given that the positive $C_{h,\mathrm{RS}}$ is even larger than C_h ($C_{h,\mathrm{RS}}/C_h > 100\%$), it is evident that the excess heat generated by molecular stress work is mainly transported from the wall to the outer region through $C_{h,\mathrm{TH}}$, in agreement with the findings of Tong et al. [20] in a supersonic zero pressure gradient turbulent boundary layer.

The $C_{h,\mathrm{RS}}$ and $C_{h,\mathrm{TH}}$ contributions are further analysed by examining the Reynolds shear stress and the wall-normal heat flux, respectively. Note that the wall-normal component of the Reynolds stress, which only contributes less than 5% to the $C_{h,\mathrm{RS}}$ contribution, can be neglected. According to Cheng et al. [51], the streamwise velocity fluctuations in the y-z plane are decomposed into four modes with increasing characteristic spanwise length scale using the BEMD method. These are denoted as u_i'', $i = 1, 2, 3, 4$. The decomposed fluctuations of the wall-normal velocity and temperature are denoted as v_i'' and T_i'', respectively. Thus, the Reynolds shear stress can be decomposed into sixteen components, rewritten as:

$$\widetilde{u''v''} = \sum_{i=1,j=1}^{4} \widetilde{u''_i v''_j}. \tag{11}$$

Each component is labelled with (i, j) to represent the contribution associated with the ith mode of the streamwise velocity fluctuations and the jth mode of the wall-normal velocity fluctuations. The components (1, 1), (2, 2), (3, 3), and (4, 4) are defined as the diagonal components, while the remaining twelve components are considered the non-diagonal components. As per Equation (9), the $C_{h,\mathrm{RS}}$ contribution can easily be decomposed as follows:

$$
\begin{aligned}
C_{h,\mathrm{RS}} = {} & \underbrace{\frac{1}{\rho_\infty u_\infty^4}\int_0^\infty -\tilde{u}\bar{\rho}\widetilde{u''_1 v''_1}\frac{\partial \tilde{u}}{\partial y}\mathrm{d}y}_{(1,1)} \\
& + \underbrace{\frac{1}{\rho_\infty u_\infty^4}\int_0^\infty -\tilde{u}\bar{\rho}\widetilde{u''_1 v''_2}\frac{\partial \tilde{u}}{\partial y}\mathrm{d}y}_{(1,2)} \\
& + \cdots \\
& + \underbrace{\frac{1}{\rho_\infty u_\infty^4}\int_0^\infty -\tilde{u}\bar{\rho}\widetilde{u''_4 v''_4}\frac{\partial \tilde{u}}{\partial y}\mathrm{d}y}_{(4,4)}.
\end{aligned}
\tag{12}
$$

Similarly, the wall-normal heat flux is broken down into sixteen separate components and expressed as follows:

$$
\widetilde{v''T''} = \sum_{i=1,j=1}^{4} \widetilde{v''_i T''_j}. \tag{13}
$$

From Equation (5), the $C_{h,\mathrm{TH}}$ contribution is then given as

$$
\begin{aligned}
C_{h,\mathrm{TH}} = {} & \underbrace{\frac{1}{\rho_\infty u_\infty^4}\int_0^\infty -c_p\bar{\rho}\frac{\partial \tilde{u}}{\partial y}\widetilde{v''_1 T''_1}\mathrm{d}y}_{(1,1)} \\
& + \underbrace{\frac{1}{\rho_\infty u_\infty^4}\int_0^\infty -c_p\bar{\rho}\frac{\partial \tilde{u}}{\partial y}\widetilde{v''_1 T''_2}\mathrm{d}y}_{(1,2)} \\
& + \cdots \\
& + \underbrace{\frac{1}{\rho_\infty u_\infty^4}\int_0^\infty -c_p\bar{\rho}\frac{\partial \tilde{u}}{\partial y}\widetilde{v''_4 T''_4}\mathrm{d}y}_{(4,4)}.
\end{aligned}
\tag{14}
$$

Regarding the scale-decomposition analysis, only the results from location s_3 for both cases are reported as the other two locations exhibit similar trends. In Figures 19–21, the pre-multiplied spanwise spectra of the decomposed velocity and temperature fluctuations (u'', v'', and T'') are displayed as functions of wall-normal distance y^+ and spanwise wavelength ${\lambda_z}^+$. The results are compared to the full spectra derived from raw DNS data. It should be noted that both the full spectra and decomposed data are normalised by their respective maximum values.

In Figure 19(a–d), there are two energetic peaks in the full spectra, one inner peak at $(y^+ = 8.9, {\lambda_z}^+ = 90)$ and one outer peak at $(y^+ = 295, {\lambda_z}^+ = 589)$. Figure 19(e–h) shows

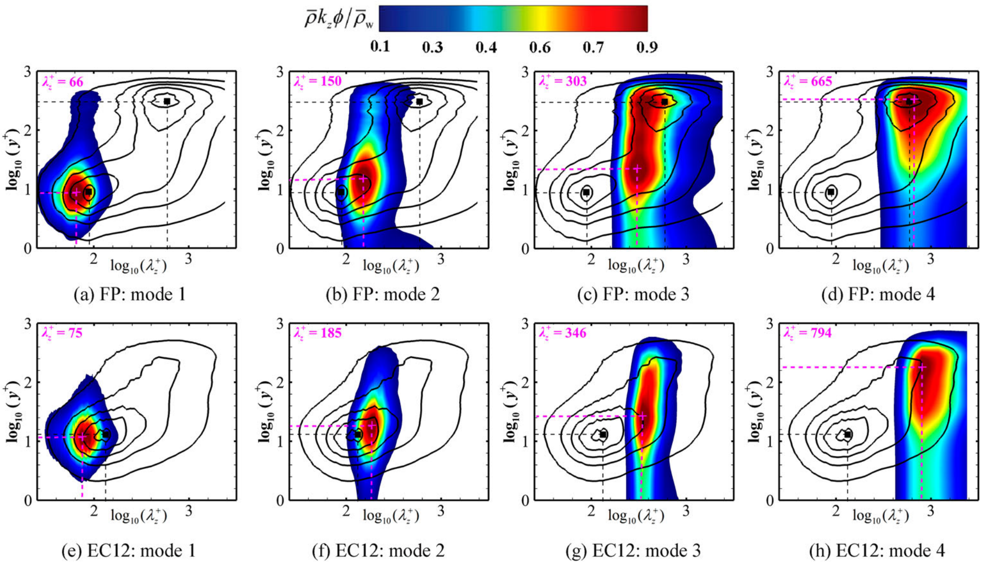

Figure 19. Pre-multiplied spanwise spectra of the decomposed streamwise velocity fluctuations u''. Isolines: DNS; contour: BEMD. Levels from 0.1 to 0.9 are shown, in steps of 0.2. Black solid square and pink cross denote the peak in the full spectra and the mode, respectively. (a) FP: mode 1; (b) FP: mode 2; (c) FP: mode 3; (d) FP: mode 4; (e) EC12: mode 1; (f) EC12: mode 2; (g) EC12: mode 3; (h) EC12: mode 4

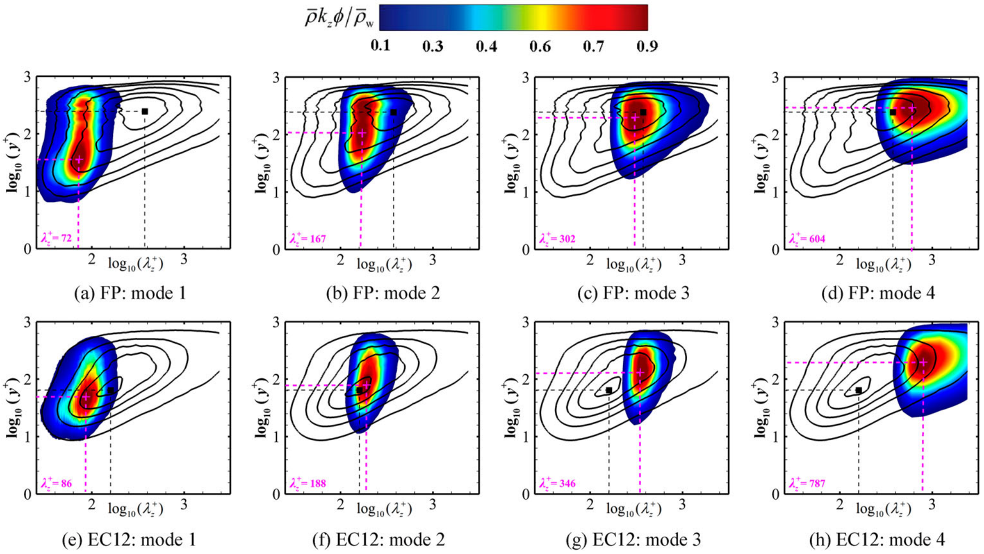

Figure 20. Pre-multiplied spanwise spectra of the decomposed wall-normal velocity fluctuations v''. See Figure 19 for the legend. (a) FP: mode 1; (b) FP: mode 2; (c) FP: mode 3; (d) FP: mode 4; (e) EC12: mode 1; (f) EC12: Mode 2; (g) EC12: mode 3; (h) EC12: mode 4.

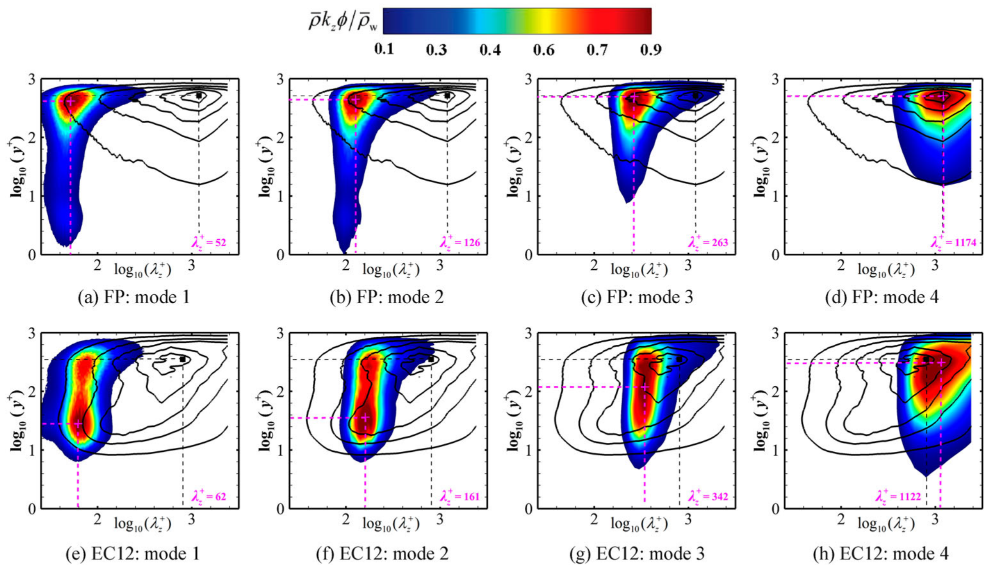

(a) FP: mode 1 (b) FP: mode 2 (c) FP: mode 3 (d) FP: mode 4

(e) EC12: mode 1 (f) EC12: mode 2 (g) EC12: mode 3 (h) EC12: mode 4

Figure 21. Pre-multiplied spanwise spectra of the decomposed temperature fluctuations T''. See Figure 19 for the legend. (a) FP: mode 1; (b) FP: mode 2; (c) FP: mode 3; (d) FP: mode 4; (e) EC12: mode 1; (f) EC12: mode 2; (g) EC12: mode 3; (h) EC12: mode 4

that the full spectra are only characterised by an inner peak at ($y^+ = 13.2$, ${\lambda_z}^+ = 129$), which is a remnant of the significantly suppressed outer-layer large-scale velocity structures. The full spectra are covered by the four BEMD modes, demonstrating the validity of the decomposition method. The first modes in Figures 19(a) and 19(e) are associated with the small-scale velocity structures in the inner region and have characteristic spanwise lengths of ${\lambda_z}^+ = 66$ and 75 for FP and EC12, respectively. The fourth modes in Figure 19(d) and 19(h) exhibit larger spanwise scales, appearing at (${\lambda_z}^+ = 665, y^+ = 339$) for FP and (${\lambda_z}^+ = 794, y^+ = 182$) for EC12, respectively, which can be interpreted as the symptom of the large-scale structures in the outer region. The other two modes represent intermediate-scale structures between the inner and outer regions.

For the wall-normal velocity fluctuations v'', a similar scenario is evident (as shown in Figure 20). Although the two full spectra show close similarities, the expansion effect greatly affects the location of the spectral peak. The full spectra for FP peaks at ($y^+ = 257$, ${\lambda_z}^+ = 372$), while for EC12, the peak is moved to $y^+ = 66$ and ${\lambda_z}^+ = 158$, indicating more energy pile-up at smaller length scales in the inner-layer region. The decomposed four modes effectively capture the overall trend of the full spectra and the characteristic spanwise length scale increases from ${\lambda_z}^+ = 72$ to ${\lambda_z}^+ = 604$ for FP and from ${\lambda_z}^+ = 86$ to ${\lambda_z}^+ = 787$ for EC12, respectively. Similarly, the temperature fluctuations T'' (whose scale decomposition is presented in Figure 21) exhibit a similar pattern to v''. The spectra of T'' for EC12 have their maxima at a much smaller spanwise length scale (${\lambda_z}^+ = 813$) in the outer region, compared to ${\lambda_z}^+ = 1174$ for FP. This suggests that the spanwise length scales of the temperature structures have generally been decreased by the expansion effect. The low-energy at the lower left part of the full spectra (observed in Figure 21(e–h)) convincingly shows the occurrence of small-scale inner-layer temperature structures inside the expanded boundary layer. Inspecting the decomposed spectra highlights the differences. The wall-normal locations of the spectral peaks for the four modes remain relatively unchanged as the mode number increases, appearing between $y^+ = 407$ and $y^+ = 501$. However, a continuous increase between the inner and outer regions is pronounced in Figure 21(e-h). This means that the first two modes shown in Figure 21(a, b) mainly characterise the small-scale temperature structures in the outer region, while those plotted in Figure 21(e, f) represent the near-wall small-scale fluctuations. The observed suppression of large-scale velocity and temperature fluctuations may be associated with the destruction of Görtler-like vortices by the expansion effect. For FP, the critical Görtler number, which is widely used to predict the formation of Görtler-like vortices, is obviously larger than the critical value of 0.6, as suggested by Loginov et al. [52] Meanwhile, the fluctuations have a dominant spanwise length scale of 0.8-1.6 times δ, which is comparable to the typical spanwise width of each vortex pair (approximately 2δ), according to Grill et al. [53] and Pasquariello et al. [54] The calculated critical Görtler number is significantly decreased for EC12, becoming much lower than the critical value, which implies the absence of Görtler-like vortices in the post-expansion region.

Figure 22 illustrates the sixteen decomposed components of Equation (11) as a function of y^+ for FP and EC12, along with the full Reynolds shear stress calculated from the raw DNS data. The sum of all the components, denoted by BEMD in the figure, coincides with the DNS data, proving the high accuracy of the decomposition method. This graph reveals two significant findings regarding the scale-dependent contributions to the Reynolds shear stress generation. First, we note that the four diagonal components have a dominant contribution compared to the twelve non-diagonal components, indicating that fluctuations in different regions of the boundary layer have a negligible effect on the two specified cases, consistent with previous findings of Cheng et al. [40] for compressible turbulent channel flows. Second, it is evident from Figure 22(a) that the (4, 4) diagonal component for FP has the maximum value at $y^+ = 300$ and dominates over the other three, highlighting the leading role of large-scale velocity fluctuations in the outer region for the Reynolds shear stress generation. In contrast, Figure 22(b) shows that the (4, 4) component is overtaken by (1, 1) and (2, 2), peaking at $y^+ = 20$ and 50, respectively, confirming the significant enhancement of small-scale inner-layer contributions to the generation for EC12 due to the influence of the expansion effect. Similarly, Figure 23 presents the decomposition of the wall-normal heat flux. The components (1, 1) and (2, 2) increase while (4, 4) decreases, yet the reduced contribution of large-scale outer-layer fluctuations still dominates for EC12. In conclusion, the decomposed results in Figures 22 and 23 demonstrate that the expansion effect elevates the role of inner small-scale structures in the Reynolds shear stress generation while suppressing the role of outer large-scale structures in the full wall-normal heat flux.

According to Equations (12) and (14), the decomposed $C_{h,\mathrm{RS}}$ and $C_{h,\mathrm{TH}}$ contributions are compared quantitatively in Figures 24 and 25, respectively. As expected, the four diagonal components dominate in Figure 24, contributing 71.18% and 65.77% of $C_{h,\mathrm{RS}}$ for FP and EC12, respectively. The component (4, 4) decreases dramatically from 41.56% to 16.77%, while the components (1, 1) and (2, 2) contribute 20.96% and 18.04% of $C_{h,\mathrm{RS}}$, respectively. Figure 25 demonstrates that despite the leading component (4, 4) from 62.82% for FP to 31.84% for EC12, it is still larger than the values for the components (1, 1) and (2, 2), which are only 10% and 12.76%, respectively. It is worth noting that the present mean

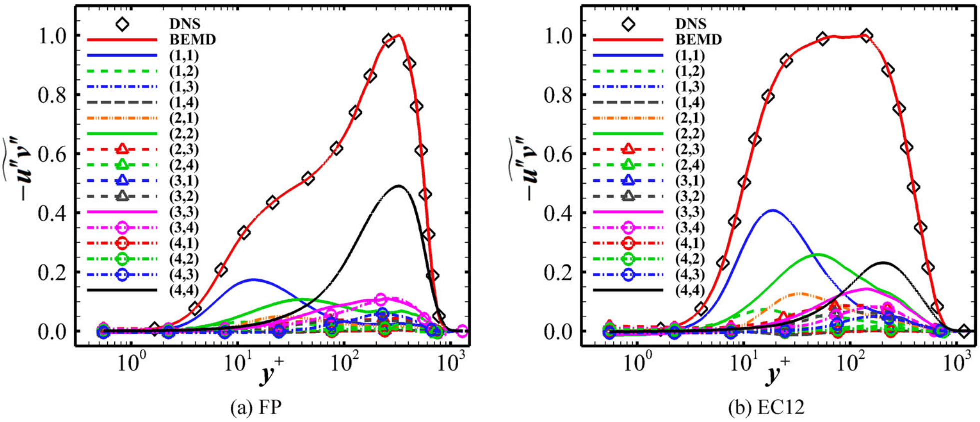

(a) FP (b) EC12

Figure 22. Decomposition of the Reynolds shear stress. (a) FP; (b) EC12.

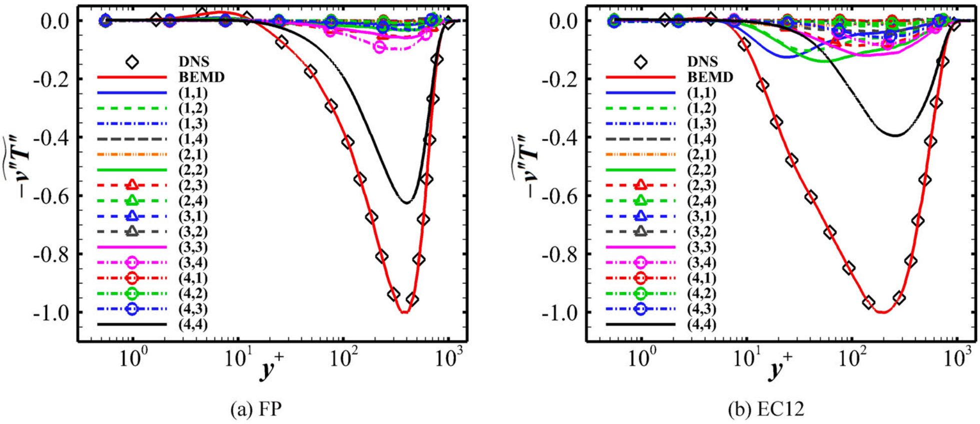

(a) FP (b) EC12

Figure 23. Decomposition of the wall-normal heat flux. (a) FP; (b) EC12.

WHF decomposition downstream of the shock-expansion interaction is similar to that at x_{ref}, which was reported by Tong et al. [13], but with obvious differences in magnitude. In their analysis, the component (4, 4) contributed 24.97% of $C_{h,\mathrm{TH}}$, which is smaller than that in the present study, while the leading contributor (1, 1) was up to 27.52% of $C_{h,\mathrm{RS}}$, which is larger than the present value. Given that the mean C_h is the same at locations S_3 and x_{ref} (see Figure 9), it can be reasonably inferred that the recovery of the outer large-scale and inner small-scale fluctuations responsible for the mean WHF generation is not fully completed in the post-expansion region.

4. Conclusions

Direct numerical simulations of impinging shock wave and supersonic turbulent boundary layer interaction over expansion corners at Mach 2.25 have been performed and compared to investigate the expansion effect on the characteristics of WHF. The results show that the mean WHF, initially increased by the impinging shock interaction, drops sharply to

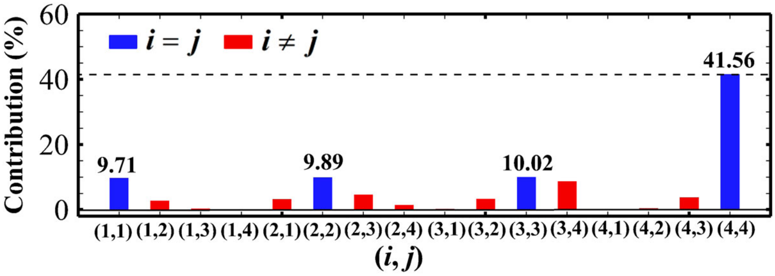

(a) FP

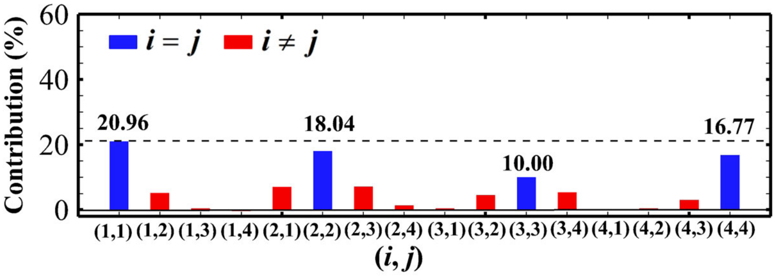

(b) EC12

Figure 24. Decomposition of the $C_{h,\mathrm{RS}}$ contribution. (a) FP; (b) EC12

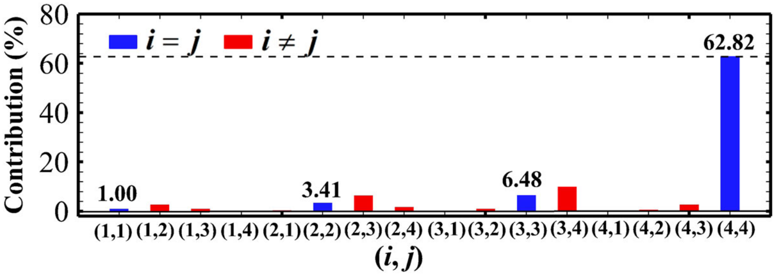

(a) FP

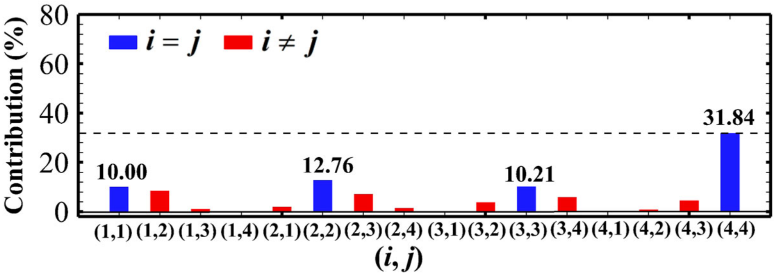

(b) EC12

Figure 25. Decomposition of the $C_{h,\mathrm{TH}}$ contribution. (a) FP; (b) EC12

its upstream value during the expansion. It is found that scaling the mean WHF with the mean wall pressure instead of the mean skin friction coefficient provides a better collapse of the curves.

The PDFs of the fluctuating WHF suggest that the expansion effect increases the occurrence probability of extreme negative events. The pre-multiplied spectra of the WHF fluctuations show an increase in high-frequency components and a decrease in intermediate-frequency components. The two-point correlation analysis reveals that the recovery of characteristic length scales in the spanwise direction is faster than that in the streamwise direction. An increased convection velocity is observed in the post-expansion region, ranging from $0.45U_\infty$ to $0.52U_\infty$. The mean WHF decomposition remains insensitive to the expansion effect. The balance between the dominant negative and positive contributions, associated with the turbulent transport of heat and the work of the Reynolds stress, remains unchanged. In addition, the scale-dependent analysis quantitatively demonstrates that the decreased large-scale structures in the outer region still dominate the turbulent transport of heat, while the contribution related to the small-scale structures in the near-wall region increases, playing a decisive role in the work of the Reynolds stress.

Disclosure statement

No potential conflict of interest was reported by the author(s).

Funding

This study was co-supported by the National Key R&D Program of China (No. 2019YFA0405300) and the National Natural Science Foundation of China (No. 11972356).

References

[1] Dolling DS. Fifty years of shockwave/boundary layer interaction research: what next? AIAA J. 2001;39(8):1517–1531. doi:10.2514/2.1476

[2] Gaitonde DV. Progress in shock wave/boundary layer interactions. Prog Aerosp Sci. 2015;72:80–99. doi:10.1016/j.paerosci.2014.09.002

[3] Clemens NT, Narayanaswamy V. Low-frequency unsteadiness of shock wave/turbulent boundary layer interactions. Annu Rev Fluid Mech. 2014;46:469–492. doi:10.1146/annurev-fluid-010313-141346

[4] Chew YT. Shockwave and boundary layer interaction in the presence of an expansion corner. Aeronautical Quarterly. 1979;30:506–527. doi:10.1017/S0001925900008684

[5] Chung KM, Lu FK. Hypersonic turbulent expansion-corner flow with shock impingement. J Propul Power. 1995;11(3):441–447. doi:10.2514/3.23863

[6] White ME, Ault DA. Expansion corner effects on hypersonic shock wave/turbulent boundary-layer interactions. J Propul Power. 1996;12(6):1169–1173. doi:10.2514/3.24157

[7] Sathianarayanan A, Verma SB. Experimental investigation of an incident shock-induced interaction near an expansion corner. J Spacecraft Rockets. 2017;54(3):769–773. doi:10.2514/1.A33466

[8] Tong FL, Li XL, Yuan XX, et al. Incident shock wave and supersonic turbulent boundary layer interactions near an expansion corner. Comput Fluids. 2020;198:104385. doi:10.1016/j.compfluid.2019.104385

[9] Zhang ZG, Tong FL, Duan JY, et al. Direct numerical simulation of supersonic turbulent expansion corner with shock impingement. Phys Fluids. 2021;33:105104. doi:10.1063/5.0064741

[10] Li WP, Fan YT, Modesti D, et al. Decomposition of the mean skin-friction drag in compressible turbulent channel flows. J Fluid Mech. 2019;875:101–123. doi:10.1017/jfm.2019.499

[11] Koll MD, Favale JV, Kirchne BM, et al. Flow structure identification in the near wake of an axisymmetric supersonic base flow using MEEMD. 47th AIAA Fluid Dynamics Conference 2017, Report No: AIAA-2017-3972.
[12] Hayashi M, Aso S, Tan A. Fluctuation of heat transfer in shock wave/turbulent boundary-layer interaction. AIAA J. 1989;27(4):399–404. doi:10.2514/3.10126
[13] Schülein E. Skin friction and heat flux measurements in shock/boundary layer interaction flows. AIAA J. 2006;44(8):1732–1741. doi:10.2514/1.15110
[14] Bernardini M, Asproulias I, Larsson J, et al. Heat transfer and wall temperature effects in shock wave turbulent boundary layer interactions. Phys Rev Fluids. 2016;1:084403. doi:10.1103/PhysRevFluids.1.084403
[15] Volpiani PS, Bernardini M, Larsson J. Effects of a nonadiabatic wall on supersonic shock/boundary -layer interactions. Phys Rev Fluids. 2018;3:083401. doi:10.1103/PhysRevFluids.3.083401
[16] Priebe S, Martin MP. Turbulence in a hypersonic compression ramp flow. Phys Rev Fluids. 2021;6:034601. doi:10.1103/PhysRevFluids.6.034601
[17] Back LH, Cuffel RF. Changes in heat transfer from turbulent boundary layers interacting with shock waves and expansion waves. AIAA J. 1970;8(10):1871–1873. doi:10.2514/3.6004
[18] Tong FL, Yuan XX, Lai J, et al. Wall heat flux in a supersonic shock wave/turbulent boundary layer interaction. Phys Fluids. 2022;34:065104. doi:10.1063/5.0094070
[19] Li XL, Fu DX, Ma YW, et al. Direct numerical simulation of compressible turbulent flows. Acta Mech Sin. 2010;26:795–806. doi:10.1007/s10409-010-0394-8
[20] Tong FL, Dong SW, Lai J, et al. Wall shear stress and wall heat flux in a supersonic turbulent boundary layer. Phys Fluids. 2022;34:015127. doi:10.1063/5.0079230
[21] Tong FL, Dong SW, Duan JY, et al. Effect of expansion on the wall heat flux in a supersonic turbulent boundary layer. Phys Fluids. 2022;34:105109. doi:10.1063/5.0113514
[22] Tong FL, Sun D, Li XL. Direct numerical simulation of impinging shock wave and turbulent boundary layer interaction over a wavy-wall. Chinese J Aeronaut. 2021;34(5):350–363. doi:10.1016/j.cja.2020.10.016
[23] Chen X, Chen JQ, Yuan XX. Hypersonic boundary layer transition on a concave wall induced by low-frequency blowing and suction. Phys Fluids. 2022;34:114105. doi:10.1063/5.0113570
[24] Wu M, Martin MP. Direct numerical simulation of supersonic turbulent boundary layer over a compression ramp. AIAA J. 2007;45(4):879–889. doi:10.2514/1.27021
[25] Gottieb S, Shu CW. Total variation diminishing Runge–Kutta schemes. Math Comput. 1998;67:73–85. doi:10.1090/S0025-5718-98-00913-2
[26] Dupont P, Haddad C, Debieve JF. Space and time organization in a shock-induced separated boundary layer. J Fluid Mech. 2006;559:255–277. doi:10.1017/S0022112006000267
[27] Sun MB, Hu ZW, Sandham ND. Recovery of s supersonic turbulent boundary layer after an expansion corner. Phys Fluids. 2017;29:076103. doi:10.1063/1.4995293
[28] Fang J, Zheltovodov AA, Yao YF, et al. On the turbulence amplification in shock-wave/turbulent boundary layer interaction. J Fluid Mech. 2020;897:A32. doi:10.1017/jfm.2020.350
[29] Pirozzoli S, Grasso F, Gatski TB. Direct numerical simulation and analysis of a spatially evolving supersonic turbulent boundary layer at $M = 2.25$. Phys Fluids. 2004;16(3):530–545. doi:10.1063/1.1637604
[30] Griffin KP, Fu L, Moin P. Velocity transformation for compressible wall-bounded turbulent flows with and without heat transfer. P Natl Acad Sci USA. 2021;118(34):e2111144118. doi:10.1073/pnas.2111144118
[31] Walz A. Compressible turbulent boundary layers (CNRS, 1962), pp. 299–350.
[32] Zhang YS, Bi WT, Hussain F, et al. A generalized Reynolds analogy for compressible wall-bounded turbulent flows. J Fluid Mech. 2014;739:392–420. doi:10.1017/jfm.2013.620
[33] Pirozzoli S, Bernardini M, Grasso F. Direct numerical simulation of transonic shock/ boundary layer interaction under conditions of incipient separation. J Fluid Mech. 2010;657:361–393. doi:10.1017/S0022112010001710

[34] Shadloo MS, Hadjadj A, Hussain F. Statistical behavior of supersonic turbulent boundary layers with heat transfer at $M_\infty = 2$. Int J Heat Fluid Flow. 2015;53:113–134. doi:10.1016/j.ijheatfluidflow.2015.02.004

[35] Humble RA, Elsinga GE, Scarano F, et al. Three-dimensional instantaneous structure of a shock wave/turbulent boundary layer interaction. J Fluid Mech. 2009;622:33–62. doi:10.1017/S0022112008005090

[36] Piponniau S, Dussauge JP, Debieve JF, et al. A simple model for low-frequency unsteadiness in shock-induced separation. J Fluid Mech. 2009;629:87–108. doi:10.1017/S0022112009006417

[37] Pirozzoli S, Grasso F. Direct numerical simulation of imping shock wave/turbulent boundary layer interaction at $M = 2.25$. Phys Fluids. 2006;18:065113. doi:10.1063/1.2216989

[38] Priebe S, Wu M, Martin MP. Direct numerical simulation of a reflected-shock-wave/turbulent-boundary-layer interaction. AIAA J. 2009;47(5):1173–1185. doi:10.2514/1.38821

[39] Back LH, Cuffel RF. Changes in heat transfer from turbulent boundary layers interacting with shock waves and expansion waves. AIAA J. 1970;8(10):1871–1873. doi:10.2514/3.6004

[40] Roy CJ, Blottner FG. Review and assessment of turbulence models for hypersonic flows. Prog Aerosp Sci. 2006;42:469. doi:10.1016/j.paerosci.2006.12.002

[41] Daniel CD, Laizet S, Vassilico JC. Wall shear stress fluctuations: mixed scaling and their effects on velocity fluctuations in a turbulent boundary layer. Phys Fluids. 2017;29:055102. doi:10.1063/1.4984002

[42] Grosse S, Schröder W. Wall-shear stress patterns of coherent structures in turbulent duct flow. J Fluid Mech. 2009;633:147–158. doi:10.1017/S0022112009007988

[43] Nottebrock B, Genurts KJ, Schröder W. Wall-shear stress measurements in an adverse pressure gradient turbulent boundary layer. 7th AIAA Flow Control Conference 2014, Report No: AIAA-2012-2978.

[44] Sreenivasan KR, Antonia RA. Properties of wall shear stress fluctuations in a turbulent duct flow. Trans ASME E: J Appl Mech. 1977;44:389–395. doi:10.1115/1.3424089

[45] Zhou Y. Rayleigh–Taylor and Richtmyer-Meshkov instability induced flow, turbulence, and mixing. I. Phys Rep. 2017;720–722:1–136.

[46] Zhou Y. Rayleigh–Taylor and Richtmyer-Meshkov instability induced flow, turbulence, and mixing. II. Phys Rep. 2017;723–725:1–160.

[47] Dupont P, Piponniau S, Dussauge J. Compressible mixing layer in shock-induced separation. J Fluid Mech. 2019;863:620–643. doi:10.1017/jfm.2018.987

[48] Bernardini M, Pirozzoli S. Wall pressure fluctuations beneath supersonic turbulent boundary layers. Phys Fluids. 2011;23:085102. doi:10.1063/1.3622773

[49] Duan L, Choudhari MM, Zhang C. Pressure fluctuations induced by a hypersonic turbulent boundary layer. J Fluid Mech. 2016;804:578–607. doi:10.1017/jfm.2016.548

[50] Sun D, Guo QL, Yuan XX, et al. A decomposition formula for the wall heat flux of a compressible boundary layer. Adv Aerodyn. 2021;3:33. doi:10.1186/s42774-021-00081-y

[51] Cheng C, Li WP, Duran AL, et al. Identity of attached eddies in turbulent channel flows with bidimensional empirical mode decomposition. J Fluid Mech. 2019;870:1037–1071. doi:10.1017/jfm.2019.272

[52] Loginov MS, Adams NA, Zheltovodov AA. Large-eddy simulation of shock-wave/turbulent-boundary-layer interaction. J Fluid Mech. 2006;565:135–169. doi:10.1017/S0022112006000930

[53] Grilli M, Hickel S, Adams NA. Large-eddy simulation of a supersonic turbulent boundary layer over a compression-expansion ramp. Int J Heat Fluid FL. 2013;42:79–93. doi:10.1016/j.ijheatfluidflow.2012.12.006

[54] Pasquariello V, Hickel S, Adams NA. Unsteady effects of strong shock-wave/boundary-layer interaction at high Reynolds number. J Fluid Mech. 2017;823:617–657. doi:10.1017/jfm.2017.308.